The Measurement of Radio Frequency Complex Permeability of Thin Round Wires

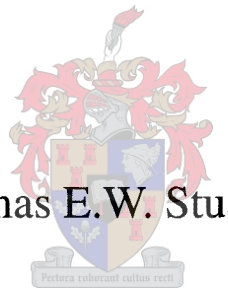

Thomas E.W. Stuart

Dissertation presented for the Degree of Doctor of Philosophy in Engineering at the University of Stellenbosch

Supervisors Prof. H.C. Reader and Prof. J.H. Cloete

April 2003

Declaration

I, the undersigned, declare that the work contained in this dissertation is my own original work, unless otherwise stated, and has not previously, in its entirety or in part, been submitted at any university for a degree.

T.E.W. Stuart December 2002

Summary

This thesis is concerned with the measurement of the complex permeability of thin round wires at radio frequencies. This is of interest as such wires are used in various applications, such as absorbing chaff. Iron and nickel alloys are also used for their good tensile properties but have an undesired electromagnetic effect which needs to be characterised. Although little work has been done in this field in recent decades it remains a relevant problem. In this thesis the advantages of accurate wide-band measurements performed by automatic network analysers are applied to the field.

The measurement system is a closed coaxial transmission line with a short circuit termination. The centre conductor is the wire of interest. The surface impedance of the wire is related to complex permeability and is measured using low-loss transmission line approximations applied to half-wavelength resonances. The loss associated with complex permeability is separated from conductivity by a D.C. conductivity measurement.

A full wave analysis of the coaxial mode was performed and compared to measured values. The maximum error of the propagation constant was found to be 31% at the highest frequencies and was primarily due to length uncertainties. By varying parameters expected error bands around the measured permeability were found. These bands are of the order 1 and demonstrate that the system is sufficiently robust.

The measurement of the permeability of two non-magnetic wires was performed and a relative permeability of 1 was found, demonstrating the correct working of the system. A steel wire was measured and compared to measurements found in literature. The permeability dropped as frequency rose as was expected, and an acceptable comparison to other measurements was made as there is no verification standard.

Thus a simple measurement system that takes advantage of calibrated automatic network analyser measurements has been developed and demonstrated to work with sufficient accuracy.

Opsomming

In hierdie tesis word die meting van die komplekse permeabiliteit van dun ronde drade by radio frekwensies ondersoek. Hierdie drade word in verskeie toepassings gebruik, waaronder dié van absorberende materiale. Nikkel- en ysterallooie word ook vir hul goeie breekkrageienskappe gebruik. In laasgenoemde gevalle moet die ongewenste elektromagnetiese effekte wat voorkom, gekarakteriseer word. Hoewel baie min werk in onlangse dekades gedoen is, bly die meting van die komplekse permeabiliteit 'n relevante probleem. In hierdie tesis word die voordele van akkurate wyeband metings, soos geneem deur 'n outomatiese netwerk analiseerder, toegepas in dié veld.

Die meetopstelling is 'n geslote koaksiale transmissielyn, kortgesluit aan een end. Die middel geleier is die draad van belang. Die oppervlak impedansie van die draad is verwant aan die komplekse permeabiliteit, en word gemeet deur die gebruik van lae verlies transmissielyn benaderings, soos toegepas op halfgolf resonante frekwensies. Die verlies wat met die komplekse permeabiliteit geassosieer word, word van die geleidingsvermoë onderskei deur 'n G.S. meting van die geleidingsvermoë.

'n Volgolf analise van die koaksiale mode is uitgevoer en met gemete waardes vergelyk. 'n Maksimum fout van 31% by die hoogste frekwensie is in die voortplantingskonstante gevind. Hierdie volg primêr uit onsekerhede in lengte. Deur die parameters te varieer kon 'n verwagte foutband rondom die gemete permeabiliteit gevind word. Hierdie bande is van die orde 1 waaruit volg dat die stelsel 'n genoegsame robuustheid toon.

Die komplekse permeabiliteit van twee nie-magnetiese drade is gemeet en 'n relatiewe permeabiliteit van 1 is gevind. Hierdie bevestig die korrekte werking van die stelsel. 'n Staal draad is opgemeet en met gepubliseerde meetresultate vergelyk. Soos verwag, verminder die permeabiliteit met 'n verhoging in frekwensie. Hoewel geen verifiëringstandaard beskikbaar is nie, is 'n aanvaarbare vergelyking met ander metings gemaak.

Die produk van die navorsing is 'n metingstelsel wat, met behulp van 'n gekalibreerde outomatiese netwerk analiseerder, aanvaarbare akkuraatheid in die meting van die komplekse permeabiliteit van dun ronde drade by radio frekwensies kan verkry.

Acknowledgements

I would like to thank Prof. Howard Reader and Prof. Johannes Cloete for their interest and support throughout my years at Stellenbosch University. Prof. Reader has always been willing to make time to provide guidance and support, while ensuring effort was directed into quality research. His generous enthusiam for educating engineers about high quality measurements was invaluable. Prof. Cloete's depth of knowledge and broad theoretical understanding ensured mathematical and scientific rigour. His interest in material properties provided the impetus for this work and kept it relevant and useful. It is an honour to have had such excellent and complementary promotors.

The staff at Central Electronic Services, particularly Wessel Croukamp and Ulrich Buttner, deserve a special mention. Mr. Buttner's useful advice and help whilst constructing the various forms of the measurement system saved much effort and time. I would also like to acknowledge Dr. Kristiaan Schreve at Central Mechanical Services who organised the measurement of the exact dimensions of the system.

I greatly appreciated Lizette Baard and the rest of the staff at the Engineering Library who tracked down obscure articles and helped me gather vital information.

This research was partly funded by the National Research Foundation and the ESKOM Tertiary Education Support programs. Their contribution to this thesis is gratefully acknowledged.

Prof. Petrie Meyer created a welcoming working environment appreciated by all the students fortunate enough to have place there. I would also like to thank him on a personal level for his friendly interest over the years.

I owe a debt of gratitude to my parents Michael and Carin, who have unwaveringly supported me in every way. I consider myself most fortunate and wish to take this opportunity thank them.

Finally, I would like to thank Claudia Brendel for her loving support. Her confidence in me and practical advice greatly helped me toward completing this task.

Contents

List of Figures

List of Tables

Chapter 1

Introduction

This thesis is concerned with the measurement of the complex permeability of thin round wires. The wires are considered to be right-circular cylinders made from a homogeneous metal where the cross-sectional diameter is less than half a millimeter.

Wires made of alloys that include iron and nickel are avoided despite their attractive tensile properties because their magnetic properties are not easy to characterise. For example, Bingle states "[v]arious attempts to measure the effective properties of the steel string in the S-band were unacceptably inaccurate. The measurement of the microwave properties of magnetic wires is an important practical problem ..." [6, p. 1624].

The ability to easily characterise a wire can also lead to the exploitation of its magnetic properties. For example, wires used in microwave absorbing materials also need to be characterised [9, p. 235].

As permeability is sensitive to the crystal structure of the metal [4, p. 249], it is not possible to measure the bulk properties of the original ingot and use these as the properties of the wire. The heating, rolling or other processes used to create the wire affect its permeability. Thus it is necessary to have a measurement system that uses the wire in its final form.

The original contribution described in this thesis is a novel system for the measurement of the complex permeability of thin round wires at radio and microwave frequencies. The system makes use of a coaxial resonator and modern vector network analyser equipment. The wideband measurements are quick to perform and require only simple construction. Error margins are included to indicate accuracy limits. The analysis of the system also included tracing the electric field lines of the Sommerfeld mode using numerical techniques. This has not previously been published and is another orignal contribution.

1.1 Historical Survey

In 1919 Arkadiew [5] published measurements of the permeability of thin round wires. These measurements were made on a parallel wire pair with a high frequency source heating a thermocouple bridge that could slide along the wires. The heating in the thermocouple was related to the energy flowing past it. In this way the absorption along the wires was measured and related to permeability. Arkadiew measured permeability at six frequencies ranging from 400 MHz to 22 GHz. The scalar permeability found by measuring attenuation is denoted μ_k.

Hoag and Jones [10] measured the permeability of thin iron wire in 1932. They also used a parallel wire system, which they short-circuited to measure resonance wavelengths. Combining this with a D.C. measurement of resistance allowed the permeability to be calculated. Their frequency range was 450 MHz – 1.4 GHz. In 1939 Hoag and Gottleib [11] measured the permeability of iron and nickel wires. They improved the previous system in several ways and covered the frequency range 98 MHz – 410 MHz. The scalar permeability found by measuring wavelength shortening is denoted μ_n.

It was found that the μ_n results were consistently lower than the μ_k results. In 1933 Arkadiew proposed that permeability could be represented by a complex number [12]. μ_k and μ_n are then related and Arkadiew could transform μ_k values to μ_n values, where he found better than expected correspondence with the values from Hoag and Jones.

In the contemporary notation used in this thesis and with a time dependency chosen as $e^{+j\omega t}$, the permeability is written as

$$\mu = \mu' - j\mu'' \tag{1.1}$$
$$= |\mu| e^{-j\delta_\mu} \tag{1.2}$$

which from Arkadiew's relations gives

$$\mu_k = |\mu| + \mu'' \tag{1.3}$$
$$\mu_n = |\mu| - \mu'' \tag{1.4}$$

Hence μ_k will be larger than μ_n when μ'' is positive. These equations allow for a comparison between complex permeability and the magnitude measurements made during the last century.

A coaxial system was used by Glathart [13] in 1939 to measure the internal inductance of thin magnetic wires. He worked at a single frequency (200 MHz) and moved a short circuit piston along the wire while measuring field strength of resonance peaks using a galvanometer. The distance between successive peaks determined the wavelength. Glathart lists several advantages that this system holds

over the open parallel wire system, which improve the accuracy of the measurement. The effects of heating and stress were also investigated.

Allanson [4] surveyed the permeability measurements that had been made by 1945. He noted that in 1903 Hagens and Rubens measured the permeability of iron at frequencies above 100 GHz and they found it to be unity. Thus it is expected that at some frequency between D.C. and optical frequencies the permeability must drop. He graphically summarised the measurements of iron, steel, nickel and cobalt, where he found large variations between different investigators. He also listed the factors that can affect the permeability:

Chemical constitution — Small changes in the percentages of the chemicals that constitute the metal can have considerable effects.

Crystal structure — Annealing, tensile stress and anisotropy can all affect the permeability.

High frequency field strength — Some researchers found that the field strength affected the permeability up to hundreds of kilohertz.

D.C. field strength — The permeability has been reduced by the application of strong external D.C. fields.

Temperature — Raising temperature raises the permeability (up to the Curie point) over a wide frequency band.

Wire radius — Arkadiew [5, Fig. 11] found a dependency of permeability on wire radius, but this may be as a result of initial permeability differences.

Allanson also provided equations for the attenuation and phase velocity of a wave in a coaxial system using surface impedance concepts. Equations similar to these are derived in this thesis for the case where μ is complex.

Bozorth [1, p. 798] summarised the most commonly used permeability measurement techniques in 1951. These consisted of a

Parallel wire system — Measurement of the ratio of A.C. to D.C. attenuation and standing wave wavelength. This system has the disadvantage of being open.

Coaxial cable — Measurement of standing wave wavelength and transmission loss. A closed coaxial system is used in this thesis.

Resonance circuit — Measurement of the inductance of the system. A measurement of only the inductance of the system cannot provide the complex permeability.

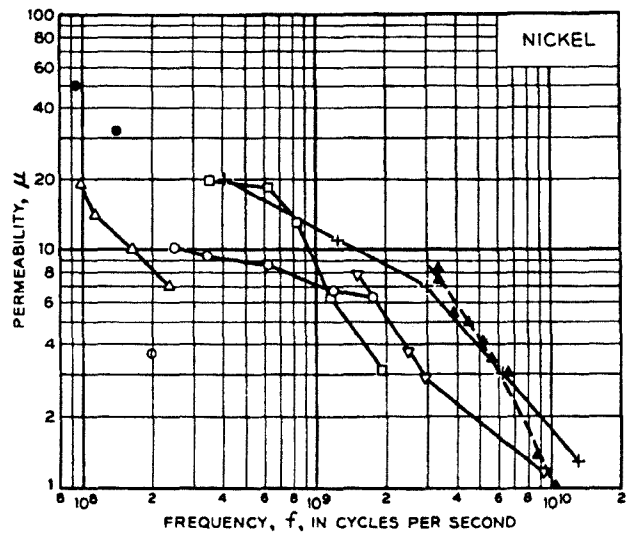

Figure 1.1: The scalar permeability of nickel at high frequencies. Source: + Arkadiew, △ Hoag and Gottleib, ⓘ Glathart, and various others (from Bozorth [1, Fig. 17–24]).

Bridge measurement of parallel wires — Direct measurement of the inductance and resistance. Bridge measurements are limited to lower frequencies.

Thermal methods — Measurement of the rise in temperature caused by energy loss. However, permeability is also dependent on temperature, making this a less accurate method.

Microwave techniques — Measurement of attenuation along waveguide or the Q of a resonating cavity. In this thesis complex permeability at microwave frequencies is partly found from the attenuation along a coaxial guide.

Bozorth also noted that the apparent permeability depends on the surface of the metal. Thin films of oxides can cause the apparent permeability to decrease by a factor of 10. The effect of magnetic fields on the sample also has a strong effect, as does the magnetic history of the sample. Fig. 1.1 (from Bozorth) shows a summary of various measurements of scalar permeability of nickel. Note that there is a large variation between different measurements. This is partly because permeability is highly dependent on the composition of the material. However the trend that the relative permeability decreases to 1 as frequency increases is evident.

Epstein also summarised permeability measurement techniques in 1954 [14]. He noted that if there is no D.C. magnetic field applied to the sample the "initial"

permeability is measured. He then showed that the concept of complex permeability is appropriate for initial permeability measurements. He also pointed out that the skin effect must be taken into account to find the intrinsic permeability of metals, as the apparent permeability would otherwise be reduced by eddy current shielding. For radio frequency permeability measurements with distributed parameter systems he suggested closed coaxial apparatus where a section of the centre wire is substituted with a magnetic wire of the same diameter. He noted that "[t]o avoid substitution errors, great care must be exercised in mechanical construction".

Complex permeability of a smooth rod was examined over a wide band and at high frequencies by Sanderson [7] in 1971. He investigated the effects of surface roughness on wave propagation by measuring the position and width of a field strength minimum on a short circuited coaxial line. A section of the inner rod of the line was substituted by a magnetic rod of the same diameter in order to find its complex permeability.

Recently much work has been done measuring the complex permeability of thin film ferrite deposits for the purposes of magnetic recording (e.g. [15]). Ferrites have been measured using, amongst other methods, cavity perturbation [16] and coaxial reflection / transmission [17] techniques. The permeability of composites made from microwires has also been measured [18]. Using a modified effective medium theory, the permeability of the composite can be related to the permeability of the individual microwires.

However, there seems to be little work on high frequency measurement techniques for highly conductive magnetic wires with diameter of the order of 0.1 mm.

1.2 Thesis Overview

In this thesis the permeability of a steel wire of unknown chemical composition is measured. It is of interest as a similar wire has been used in separate experiments [6, p. 1624] and hence its properties can be compared to expected values. This is necessary as there is no verification standard for the complex permeability of wires. The field strengths of the measurement are small and the measurement is made at room temperature.

A coaxial cavity is used to measure the surface impedance of the inner wire. The cavity is shown in Fig. 1.2. The cavity is terminated by a good short circuit and will resonate when its electrical length is a multiple of half or quarter of a wavelength of excitation. This electrical length is dependent on the geometry of the system as well as the materials from which the cavity is constructed. Thus the frequencies at which resonance occurs are affected, in part, by the internal inductance of the thin round wire. At the same time the input resistance at half-

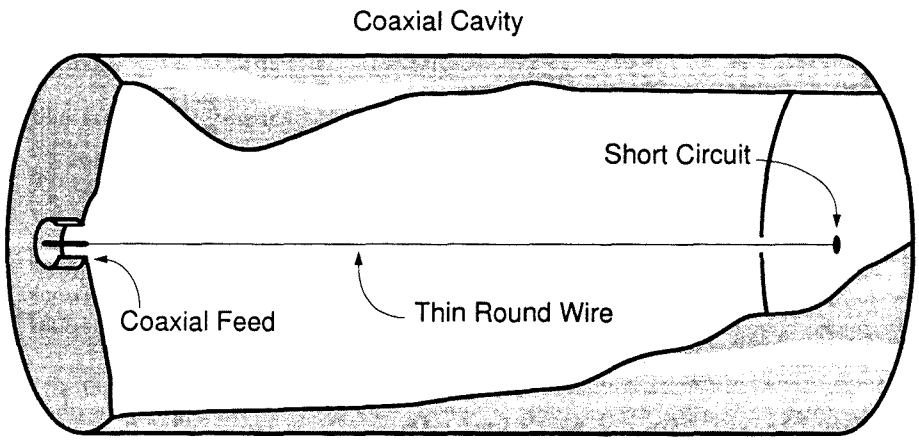

Figure 1.2: Geometry of the coaxial resonant cavity used for measurements in this thesis.

wavelength resonances deviates from the ideal zero due to the surface resistance of the wire. In this way the surface impedance can be measured and related to the complex permeability of the inner wire.

In Chapter 2 Maxwell's equations are solved subject to boundary conditions in the cavity. In order to characterise the electromagnetic fields in the cavity, Maxwell's equations must be solved in cylindrical coordinates. The conductivity and permeability are modelled in the frequency domain, and the field distributions in the cavity are established. The dominant mode in the cavity is shown to be transverse magnetic, allowing a coaxial feed to be used to excite the mode.

In Chapter 3 the measurement system is described. The resonance measurement is related to the surface impedance of the wire, which is in turn related to the complex permeability. Time-domain gating is used to remove the effect of the evanescent modes excited at the junction between the feed and the cavity. A sensitivity analysis is also performed and various improvements suggested by this analysis are made.

In Chapter 4 measurement results from three wires, two non-magnetic and the other magnetic, are shown. The measured wavenumber is compared to the predicted wavenumber from the full-wave analysis performed in Chapter 2. The accuracy of the measurements is also discussed and error bars are used to show the degree of variations expected.

The thesis concludes with Chapter 5 where the results are discussed and the applicability of the measurement technique is evaluated against other methods. Future work is also suggested.

Chapter 2

Coaxial Field Distribution

A full wave analysis of the coaxial system is performed in this chapter. The solution is found in the frequency domain and conductivity and complex permeability are introduced into Maxwell's equations. It is shown that Hertzian vector potentials transform this vector problem into a scalar Helmholtz equation, which is solved subject to cylindrical boundary conditions. First a two-layer structure (a single wire in free space) is solved and the electric field lines of this Sommerfeld mode are plotted. The problem is then expanded to a three-layer coaxial system and the characteristic wavenumber equation is found. Finally small and large argument approximations are applied to this characteristic equation to find good initial positions for the numerical root finder.

2.1 Maxwell's Equations with Conductivity and Permeability

Maxwell's equations are written in the frequency domain and loss is introduced as conductivity and complex permeability. With the time phasor defined as $e^{+j\omega t}$ Ampère's law is written as

$$\begin{aligned} \nabla \times \mathbf{H} &= \mathbf{J}_s + [\sigma + j\omega\varepsilon_0 (1 + \chi_e)]\,\mathbf{E} \\ &= \mathbf{J}_s + j\omega\varepsilon\mathbf{E} \end{aligned} \tag{2.1}$$

where the bold symbols are phasors. $\mathbf{H}$ is the magnetic field, $\mathbf{E}$ is the electric field, $\mathbf{J}_s$ is the source electric current density, σ is the conductivity of the medium, ε_0 is the permittivity of free space, ω is the radian frequency and χ_e is the dielectric susceptibility of the medium. Equation (2.1) uses the assumptions of a simple linear isotropic medium, which apply to all the materials used in the measurements.

The permittivity is separated into real and imaginary parts, where the imaginary part corresponds to loss [19, §6.4].

$$\begin{aligned} \varepsilon &= \varepsilon_0\varepsilon_r - \mathrm{j}\frac{\sigma}{\omega} \quad (\varepsilon_r = 1 + \chi_e) \\ &= \varepsilon' - \mathrm{j}\varepsilon'' \end{aligned} \tag{2.2}$$

where it is also assumed that the susceptibility of the medium is real and loss associated with electric fields is attributed to conductivity.

The materials used are good conductors, so the additional approximation can be made that the conductivity dominates the permittivity below the millimetre wavelength range.

$$\frac{\sigma}{\omega} \gg \varepsilon_0\varepsilon_r \implies \varepsilon \approx -\mathrm{j}\frac{\sigma}{\omega} \tag{2.3}$$

Hence ε is purely imaginary and in a source-free region Ampère's law becomes

$$\nabla \times \mathbf{H} \approx \sigma\mathbf{E} \tag{2.4}$$

Taking the curl of (2.4) leads to

$$\nabla \cdot \mathbf{E} = 0 \tag{2.5}$$

which shows that there is no free charge density in a good conductor.

Faraday's law is written as

$$\nabla \times \mathbf{E} = -\mathrm{j}\omega\mu_0 (\mathbf{H} + \mathbf{M}) \tag{2.6}$$

$$= -\mathrm{j}\omega\mu\mathbf{H} \tag{2.7}$$

where μ_0 is the permeability of free space and $\mathbf{M}$ is the magnetic polarisation. In order to introduce magnetic loss into the system, μ is made complex.

$$\mu = \mu' - \mathrm{j}\mu'' \tag{2.8}$$

$$= \mu_0 (\mu_r' - \mathrm{j}\mu_r'') \tag{2.9}$$

$$= |\mu| \mathrm{e}^{-\mathrm{j}\delta_\mu} \tag{2.10}$$

Taking the curl of Faraday's law in a source-free homogeneous region gives

$$\nabla \times \nabla \times \mathbf{E} = \nabla(\nabla \cdot \mathbf{E}) - \nabla^2\mathbf{E} = -\mathrm{j}\omega\mu\nabla \times \mathbf{H} \tag{2.11}$$

$$\implies \nabla^2\mathbf{E} \approx \mathrm{j}\omega\mu\nabla \times \mathbf{H} \tag{2.12}$$

$$\approx \mathrm{j}\omega\mu\sigma\mathbf{E} \tag{2.13}$$

where (2.5) has been used. This can be written as

$$\nabla^2\mathbf{E} - k^2\mathbf{E} = 0 \tag{2.14}$$

where k is the wavenumber. Thus substituting the conductivity and permeability for a lossy source-free homogeneous region into the Helmholtz equation [19, §7.2] gives the wavenumber for a uniform plane wave

$$k^2 = \omega^2\mu\varepsilon \tag{2.15}$$
$$= -\mathrm{j}\omega\mu_0(\mu_r' - \mathrm{j}\mu_r'')\sigma \tag{2.16}$$

2.2 Hertzian Vector Potentials

The fields are found using Hertzian electric and magnetic vector potentials, $\mathbf{\Pi}^e$ and $\mathbf{\Pi}^m$ [20, §4–1]. Electromagnetic wave propagation is assumed to be in the $\hat{z}$ direction, which allows for the simplification of the vector potentials into scalar potentials. This also divides the modes into transverse electric (TE) and transverse magnetic (TM) to the $\hat{z}$ direction.

The TM modes are found from the scalar Hertzian electric potential (2.17) and the TE modes are found from the scalar Hertzian magnetic potential (2.18).

In the coaxial transmission line the dominant mode is quasi-TEM. This mode is TM but, owing to the loss in the conducting walls, not quite TE. The feed system is also coaxial and the junction does not excite TE modes. Thus the only modes that are of interest are TM modes and the magnetic vector potential is set to zero.

$$\mathbf{\Pi}^e = \Pi_z^e\hat{z} \tag{2.17}$$
$$\mathbf{\Pi}^m = 0 \tag{2.18}$$

The fields are related to the electric scalar potential as

$$\mathbf{E} = \nabla\left[\nabla\cdot(\Pi_z^e\hat{z})\right] + \omega^2\mu\varepsilon\Pi_z^e\hat{z} \tag{2.19}$$
$$\mathbf{H} = \mathrm{j}\omega\varepsilon\left[\nabla\times(\Pi_z^e\hat{z})\right] \tag{2.20}$$

and the scalar potential Π_z^e is subject to the scalar Helmholtz equation

$$\nabla^2\Pi_z^e + k^2\Pi_z^e = 0 \tag{2.21}$$

where the wavenumber is given by (2.15) and contains information about the electrical properties of the medium.

2.3 Solving for the Potentials in Cylindrical Coordinates

Solving Maxwell's equations in the cylindrical coordinate system requires Bessel functions. The cylindrical coordinate system is shown in Fig. 2.1.

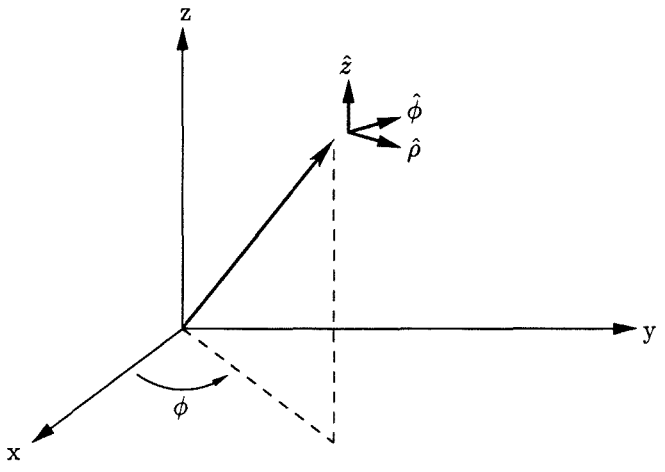

Figure 2.1: Cylindrical coordinate system showing unit vectors.

In cylindrical coordinates the Helmholtz equation (2.21) is written as

$$\frac{1}{\rho}\frac{\partial}{\partial\rho}\left(\rho\frac{\partial\Pi_z^e}{\partial\rho}\right)+\frac{1}{\rho^2}\frac{\partial^2\Pi_z^e}{\partial\phi^2}+\frac{\partial^2\Pi_z^e}{\partial z^2}+k^2\Pi_z^e=0 \tag{2.22}$$

Separation of variables is used to form three interrelated ordinary differential equations. Let

$$\Pi_z^e = R(\rho)\Phi(\phi)Z(z) \tag{2.23}$$

$$\Longrightarrow \rho\frac{\mathrm{d}}{\mathrm{d}\rho}\left(\rho\frac{\mathrm{d}R}{\mathrm{d}\rho}\right)+\left[(k_\rho\rho)^2-n^2\right]R = 0, \tag{2.24}$$

$$\frac{\mathrm{d}^2Z}{\mathrm{d}z^2}+k_zZ = 0, \tag{2.25}$$

$$\frac{\mathrm{d}^2\Phi}{\mathrm{d}\phi^2}+n^2\Phi = 0 \tag{2.26}$$

where

$$k^2=n^2+k_\rho^2+k_z^2 \tag{2.27}$$

relates the wavenumbers in the three dimensions of the coordinate system.

Equation (2.24) is Bessel's differential equation [21, §5.4], while (2.25) and (2.26) are simple second-order ordinary differential equations with harmonic (exponential or sinusoidal) solutions. Some solutions to Bessel's equation are listed in Table 2.1. The appropriate solution is chosen according to expected wave behaviour.

Table 2.1: Bessel functions and electromagnetic wave interpretations [8, Table 5–1, p. 203].

Bessel Function	***Interpretation***
$J_n(k_\rho\rho)$ Bessel Function of the First Kind	Standing wave (defined at $\rho = 0$)
$N_n(k_\rho\rho)$ Bessel Function of the Second Kind	Standing wave (undefined at $\rho = 0$)
$H_n^{(1)}(k_\rho\rho) = J_n(k_\rho\rho) + \mathrm{j}N_n(k_\rho\rho)$ Hankel Function of the First Kind	Travelling wave in the $-\rho$ direction
$H_n^{(2)}(k_\rho\rho) = J_n(k_\rho\rho) - \mathrm{j}N_n(k_\rho\rho)$ Hankel Function of the Second Kind	Travelling wave in the $+\rho$ direction

The field distributions of interest are quasi-TEM and the feed junction of the system is symmetric and does not excite modes with azimuthal variations. Thus the fields are taken to have no ϕ variation and n is chosen as zero.

The scalar electric potential is found from (2.23) as

$$\Pi_z^e = [A_1 B_0(k_\rho\rho) + A_2 Z_0(k_\rho\rho)]\, \mathrm{e}^{\pm \mathrm{j}k_z z} \tag{2.28}$$

where A_1 and A_2 are constants, B_0 and Z_0 are any Bessel functions order 0 and travelling waves are assumed in the $\pm\hat{z}$ directions.

The E_z and H_ϕ fields are chosen to satisfy boundary conditions at interfaces in the following sections. These fields are derived from the scalar potential in cylindrical coordinates using (2.19) and (2.20) as

$$E_z = \frac{\partial^2 \Pi_z^e}{\partial z^2} + \mu\varepsilon\omega^2 \Pi_z^e = (-k_z^2 + k^2)\Pi_z^e \tag{2.29}$$

$$= k_\rho^2 \Pi_z^e \tag{2.30}$$

$$H_\phi = -\mathrm{j}\omega\varepsilon \frac{\partial \Pi_z^e}{\partial \rho} \tag{2.31}$$

2.4 The Sommerfeld Mode

As a first step toward solving for the fields in the three-layer coaxial cavity, a simpler structure was examined. The three-layer structure was reduced to a two-layer

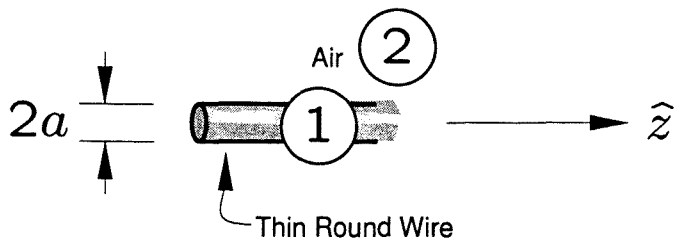

Figure 2.2: Geometry of a round conductive wire in free space.

structure consisting of a thin round wire surrounded by free space. Fig. 2.2 shows the geometry of this two-layer system. The Sommerfeld mode is the dominant surface wave mode found on round wires with finite conductivity in free space, and is a TM wave with no variation in the ϕ direction [2]. Air is assumed to have the dielectric properties of free space.

2.4.1 Wavenumber of the Sommerfeld Mode

The fields are found by treating the wire and the surrounding medium as a two-dielectric medium. At the interface between the media the tangential field intensities must be continuous. Applying these boundary conditions leads to an equation whose roots are the $\hat{z}$-directed wavenumber, k_z.

The scalar potentials must be chosen for each region from (2.28). As there is no ϕ variation, $n = 0$ in both regions. In region 1 (the thin round wire) a standing wave is expected, which should be defined at $\rho = 0$. From Table 2.1 a Bessel function of the first kind is chosen. In region 2 (air) a wave travelling radially away from the wire is expected, and hence a Hankel function of the second kind is used. Thus the Hertzian scalar electric potentials in both regions for a wave travelling in the $+\hat{z}$ direction are

$$\Pi^e_{z1} = AJ_0(k_{\rho 1}\rho)\mathrm{e}^{-\mathrm{j}k_z z} \tag{2.32}$$

$$\Pi^e_{z2} = BH_0^{(2)}(k_{\rho 2}\rho)\mathrm{e}^{-\mathrm{j}k_z z} \tag{2.33}$$

where A and B are constants and the subscripts 1 and 2 indicate quantities in regions 1 and 2 respectively.

Matching the E_z fields at $\rho = a$ leads to the relation

$$k_{\rho 1}^2 AJ_0(k_{\rho 1}a)\mathrm{e}^{-\mathrm{j}k_z z} = k_{\rho 2}^2 BH_0^{(2)}(k_{\rho 2}a)\mathrm{e}^{-\mathrm{j}k_z z}$$

$$\Longrightarrow \frac{A}{B} = \frac{k_{\rho 2}^2}{k_{\rho 1}^2}\frac{H_0^{(2)}(k_{\rho 2}a)}{J_0(k_{\rho 1}a)} \tag{2.34}$$

Matching the H_ϕ fields at $\rho = a$ leads to a similar relation

$$\begin{aligned} & \mathrm{j}\omega\varepsilon_1 k_{\rho 1} A J_1(k_{\rho 1}a)\mathrm{e}^{-\mathrm{j}k_z z} = \mathrm{j}\omega\varepsilon_2 k_{\rho 2} B H_1^{(2)}(k_{\rho 2}a)\mathrm{e}^{-\mathrm{j}k_z z} \\ \Longrightarrow \quad & \frac{A}{B} = \frac{\varepsilon_2 k_{\rho 2}}{\varepsilon_1 k_{\rho 1}} \frac{H_1^{(2)}(k_{\rho 2}a)}{J_1(k_{\rho 1}a)} \end{aligned} \tag{2.35}$$

Combining (2.34) and (2.35) results in a transcendental characteristic equation which has roots which give k_z for the Sommerfeld mode.

$$\boxed{\frac{k_{\rho 1}}{\varepsilon_1}\frac{J_0(k_{\rho 1}a)}{J_1(k_{\rho 1}a)} - \frac{k_{\rho 2}}{\varepsilon_2}\frac{H_0^{(2)}(k_{\rho 2}a)}{H_1^{(2)}(k_{\rho 2}a)} = 0} \tag{2.36}$$

where

$$k_{\rho 1} = \left(k_1^2 - k_z^2\right)^{\frac{1}{2}} \tag{2.37}$$

$$k_{\rho 2} = \left(k_2^2 - k_z^2\right)^{\frac{1}{2}} \tag{2.38}$$

The equations for the radial wavenumbers k_ρ require a choice of sign. It can be argued that a radial wave propagating outwards in a lossy medium must be attenuated. Thus the magnitude of $H_n^{(2)}(k_\rho\rho)$ must decrease to zero as $\rho \to \infty$ which requires the sign of the imaginary part of k_ρ to be negative.

The radial wavenumber in the thin round wire has large real and imaginary components as can be seen from

$$k_{\rho 1} = +\sqrt{k_1^2 - k_z^2} \tag{2.39}$$

where for a good conductor in region 1

$$|k_1^2| \gg |k_z^2| \tag{2.40}$$

Thus

$$k_{\rho 1} \approx \sqrt{-\mathrm{j}\omega\mu_1\sigma_1} \tag{2.41}$$

$$= \frac{1}{\delta_1} - \mathrm{j}\frac{1}{\delta_1} \tag{2.42}$$

where

$$\delta_1 = \frac{1}{\sqrt{\pi f \mu_1 \sigma_1}} \tag{2.43}$$

is the skin depth in region 1.

Unfortunately δ_1 becomes a small number for a good conductor as frequency rises, resulting in large complex arguments in the Bessel functions on the left hand

Table 2.2: Comparison of k_z from various sources (a = 1 mm; f = 1 GHz; σ = 5.8×10^7 S/m).

k_z	Source
$20.960 - \mathrm{j}1.3413 \times 10^{-3}$	Stratton (from Sommerfeld) [3, p. 530]
$20.979 - \mathrm{j}2.2935 \times 10^{-2}$	Goubau [23, Design Graphs]
$20.9597235 - \mathrm{j}1.4099925 \times 10^{-3}$	Least-Squares Routine

side of (2.36). Large argument approximations for these functions are shown in Appendix A.

The zeros of (2.36) were found using a least-squares search function `lsqnonlin` [22, Optimization Toolbox Reference]. This is a multivariable zero finder which was set to use a medium-scale, Levenberg-Marquardt method with line search. The real and imaginary parts of k_z were treated as two variables. Typically 10 iterations with 60 function evaluations were required per frequency point in order for the tolerance on k_z to be less that 10^{-12}.

Sommerfeld made large and small argument approximations to solve (2.36) [2] while Goubau [23] created design graphs in order to solve similar equations. Table 2.2 lists various values of k_z found using different techniques.

2.4.2 Electric field lines of the Sommerfeld mode

Included in Sommerfeld's work is a diagram of electric field lines [2, Fig. 5]. In 1941, Stratton also "pictured roughly" the electric field lines associated with the Sommerfeld mode [3, Fig. 104]. Both these diagrams are shown in Fig. 2.3.

The electric field lines of the Sommerfeld mode were found using numerical techniques by solving the ordinary differential equation that describes the tangent to the field line:

$$\frac{\mathrm{d}\rho}{\mathrm{d}z} = \frac{e_\rho}{e_z} \tag{2.44}$$

where e_ρ and e_z are electric field components in the time domain, e.g. [19, p. 455]. The time $t = 0$ is chosen throughout this section.

The Matlab toolbox ODESUITE was used to solve (2.44). These lines were found using the `ode23t` solver. This is a low accuracy solver that has no numerical damping, for problems that are moderately stiff. It is an implementation of the trapezoidal rule using a free interpolant [24, p. 2–548]. The tolerances were set to an order smaller than the defaults.

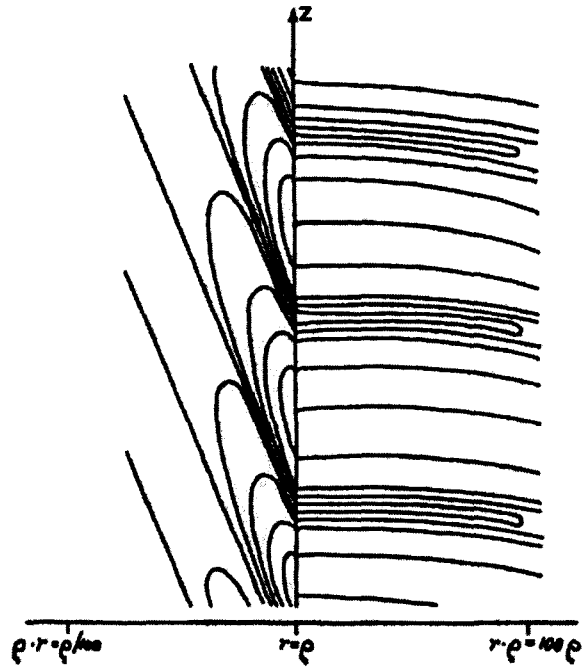

(a) Sommerfeld

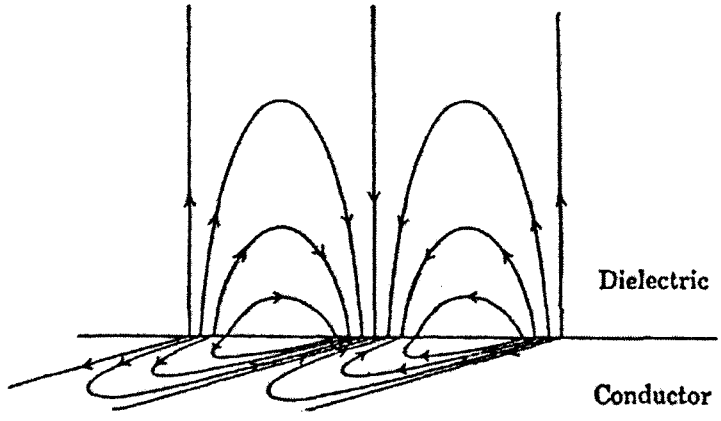

(b) Stratton

Figure 2.3: Electric field lines, in planes containing the wire axis, of the Sommerfeld mode according to: (a) Sommerfeld [2, Fig. 5] with propagation in the $-\hat{z}$ direction (metal on the left of the $\hat{z}$ axis, air on the right); and (b) Stratton [3, Fig. 104] with propagation from left to right. Stratton's sketch does not satisfy tangential electric field continuity at the interface, as can be seen from the lines terminating at infinity.

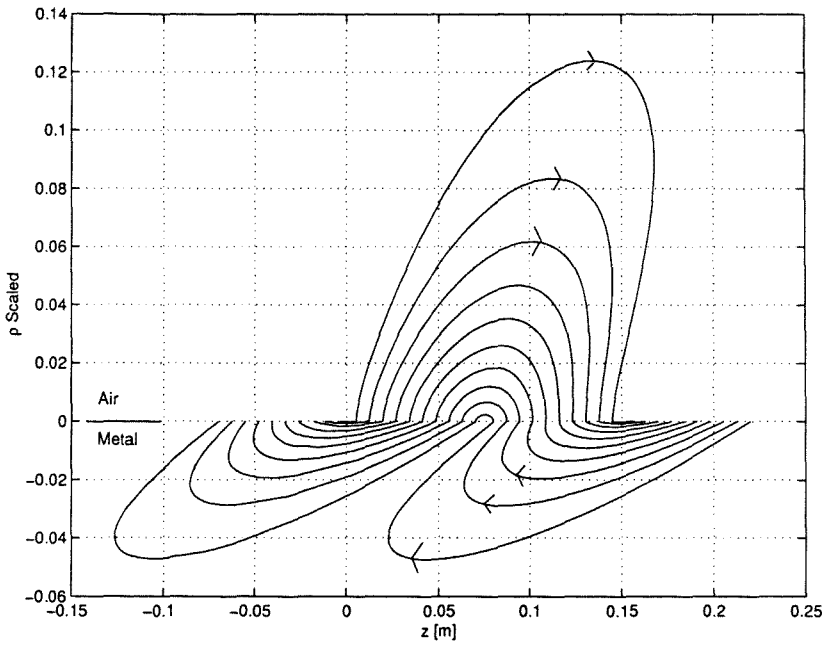

Figure 2.4: Combined scaled electric field lines of the Sommerfeld mode found using numerical techniques.

Fig. 2.4 shows a combination of the scaled electric field lines in each region. Comparison of this diagram to the field lines drawn by Sommerfeld and Stratton (Fig. 2.3) shows that Stratton's field lines are inaccurate. At the interface between the dielectric and the metal the tangential electric field must be continuous which is not the case for Stratton's diagram. On the other hand, the numerical process provides graphs that have the same form as was estimated by Sommerfeld in 1899!

2.5 Coaxial Cable

2.5.1 Quasi-TEM Coaxial Wavenumber Equation

The coaxial system consists of three layers, as shown in Fig. 2.5. Initially the reflection / transmission matrix formulation by Chew [25, Ch. 3] was used to solve for the wavenumber. However this method was found to be unnecessarily general and cumbersome. Instead an approach similar to [20, §4.11] was taken. This approach simply expands the technique used in §2.4 to three layers.

The $\hat{z}$-directed wavenumber is found as in the previous section, by enforcing

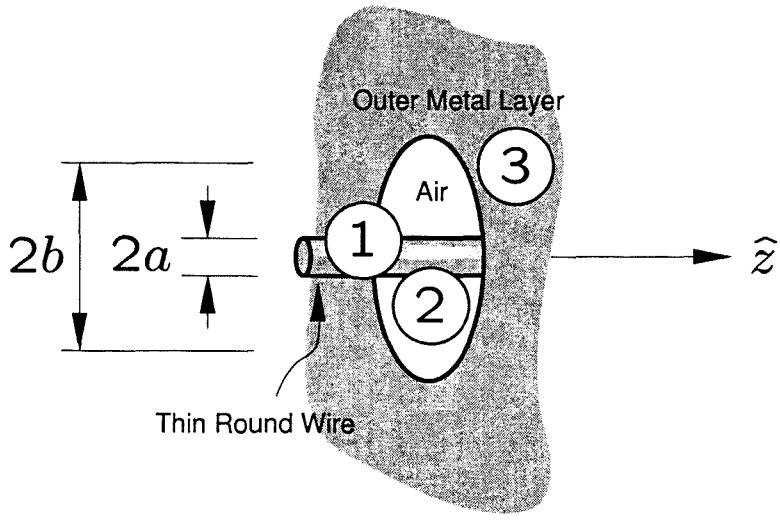

Figure 2.5: Geometry of a coaxial (three-layer) cable.

the continuity of tangential field components. Only the dominant (TM) mode is found. The appropriate scalar potential functions are chosen as

$$\Pi_{z1}^{e} = AJ_0(k_{\rho 1}\rho)\mathrm{e}^{-\mathrm{j}k_z z} \tag{2.45}$$

$$\Pi_{z2}^{e} = B\left[H_0^{(2)}(k_{\rho 2}\rho) + CJ_0(k_{\rho 2}\rho)\right]\mathrm{e}^{-\mathrm{j}k_z z} \tag{2.46}$$

$$\Pi_{z3}^{e} = DH_0^{(2)}(k_{\rho 3}\rho)\mathrm{e}^{-\mathrm{j}k_z z} \tag{2.47}$$

where two Bessel functions are required in the air region and A, B, C and D are constants.

Applying the continuity of tangential fields at the interfaces a and b leads to

$$C = -\frac{H_0^{(2)}(k_{\rho 2}a) - \frac{\varepsilon_2}{\varepsilon_1}\frac{k_{\rho 1}}{k_{\rho 2}}\frac{J_0(k_{\rho 1}a)}{J_1(k_{\rho 1}a)}H_1^{(2)}(k_{\rho 2}a)}{J_0(k_{\rho 2}a) - \frac{\varepsilon_2}{\varepsilon_1}\frac{k_{\rho 1}}{k_{\rho 2}}\frac{J_0(k_{\rho 1}a)}{J_1(k_{\rho 1}a)}J_1(k_{\rho 2}a)} \tag{2.48}$$

and

$$C = -\frac{H_0^{(2)}(k_{\rho 2}b) - \frac{\varepsilon_2}{\varepsilon_3}\frac{k_{\rho 3}}{k_{\rho 2}}\frac{H_0^{(2)}(k_{\rho 3}b)}{H_1^{(2)}(k_{\rho 3}b)}H_1^{(2)}(k_{\rho 2}b)}{J_0(k_{\rho 2}b) - \frac{\varepsilon_2}{\varepsilon_3}\frac{k_{\rho 3}}{k_{\rho 2}}\frac{H_0^{(2)}(k_{\rho 3}b)}{H_1^{(2)}(k_{\rho 3}b)}J_1(k_{\rho 2}b)} \tag{2.49}$$

These can be combined to find the characteristic wavenumber equation for the

coaxial quasi-TEM mode:

$$\frac{\frac{k_{\rho 2}}{\varepsilon_2}\frac{H_0^{(2)}(k_{\rho 2}a)}{H_1^{(2)}(k_{\rho 2}a)} - \frac{k_{\rho 1}}{\varepsilon_1}\frac{J_0(k_{\rho 1}a)}{J_1(k_{\rho 1}a)}}{\frac{k_{\rho 2}}{\varepsilon_2}\frac{J_0(k_{\rho 2}a)}{J_1(k_{\rho 2}a)} - \frac{k_{\rho 1}}{\varepsilon_1}\frac{J_0(k_{\rho 1}a)}{J_1(k_{\rho 1}a)}}\frac{H_1^{(2)}(k_{\rho 2}a)}{J_1(k_{\rho 2}a)} = \frac{\frac{k_{\rho 2}}{\varepsilon_2}\frac{H_0^{(2)}(k_{\rho 2}b)}{H_1^{(2)}(k_{\rho 2}b)} - \frac{k_{\rho 3}}{\varepsilon_3}\frac{H_0^{(2)}(k_{\rho 3}b)}{H_1^{(2)}(k_{\rho 3}b)}}{\frac{k_{\rho 2}}{\varepsilon_2}\frac{J_0(k_{\rho 2}b)}{J_1(k_{\rho 2}b)} - \frac{k_{\rho 3}}{\varepsilon_3}\frac{H_0^{(2)}(k_{\rho 3}b)}{H_1^{(2)}(k_{\rho 3}b)}}\frac{H_1^{(2)}(k_{\rho 2}b)}{J_1(k_{\rho 2}b)} \tag{2.50}$$

This characteristic wavenumber equation can be linked to the Sommerfeld wavenumber equation (2.36) by taking the limit as $b \to \infty$. From the large argument approximations in Appendix A the right hand side of (2.50) can be written as

$$\lim_{b\to\infty} \frac{\frac{k_{\rho 2}}{\varepsilon_2}\frac{H_0^{(2)}(k_{\rho 2}b)}{H_1^{(2)}(k_{\rho 2}b)} - \frac{k_{\rho 3}}{\varepsilon_3}\frac{H_0^{(2)}(k_{\rho 3}b)}{H_1^{(2)}(k_{\rho 3}b)}}{\frac{k_{\rho 2}}{\varepsilon_2}\frac{J_0(k_{\rho 2}b)}{J_1(k_{\rho 2}b)} - \frac{k_{\rho 3}}{\varepsilon_3}\frac{H_0^{(2)}(k_{\rho 3}b)}{H_1^{(2)}(k_{\rho 3}b)}}\frac{H_1^{(2)}(k_{\rho 2}b)}{J_1(k_{\rho 2}b)} \tag{2.51}$$

$$= \frac{\frac{k_{\rho 3}}{\varepsilon_3} - \frac{k_{\rho 2}}{\varepsilon_2}}{\frac{k_{\rho 3}}{\varepsilon_3} + \frac{k_{\rho 2}}{\varepsilon_2}} \lim_{b\to\infty} \frac{H_1^{(2)}(k_{\rho 2}b)}{J_1(k_{\rho 2}b)} \tag{2.52}$$

$$= \frac{\frac{k_{\rho 3}}{\varepsilon_3} - \frac{k_{\rho 2}}{\varepsilon_2}}{\frac{k_{\rho 3}}{\varepsilon_3} + \frac{k_{\rho 2}}{\varepsilon_2}} \mathrm{j}\sqrt{\mathrm{j}} \lim_{b\to\infty} \frac{\mathrm{e}^{+\mathrm{j}k_{\rho 2}b}}{\sin(k_{\rho 2}b - \frac{\pi}{4})} \tag{2.53}$$

$$= 0 \tag{2.54}$$

as $k_{\rho 2}$ has a negative imaginary part. Hence (2.50) becomes the Sommerfeld mode wavenumber equation for $b \to \infty$.

2.5.2 Numerical Solution of the Quasi-TEM Coaxial Wavenumber Equation

The solution to (2.50) was found numerically using the `lsqnonlin` function least-squares routine, as was done with the Sommerfeld mode. However, there are two complications. Firstly, k_z is related to the radial wavenumber in the air region by a square root function that introduces a branch cut close to the zero:

$$k_{\rho 2} = -\sqrt{k_2^2 - k_z^2} \tag{2.55}$$

A discontinuity caused by crossing the cut prevents root finder convergence. Some effort was spent using Riemann surfaces [20, p. 586] to remove the discontinuity,

but ultimately it was found that the branch cut can be avoided simply by solving for $k_{\rho 2}$ instead of k_z. The radial wavenumbers in the metal regions are related to $k_{\rho 2}$ by (2.27). Once $k_{\rho 2}$ is known, k_z can be found from (2.55).

The second problem is that the region of good initial positions for solving for $k_{\rho 2}$ is small, so the initial position must be chosen with care. In order to find such positions, small argument approximations are made on (2.50) following Stratton (see Appendix A).

For a low-loss system, $k_z \approx k_2$ and hence from (2.55) $k_{\rho 2}$ is small. The radii a and b are also considered small and thus small argument approximations can be taken for these terms in (2.50):

$$\frac{-\frac{k_{\rho 2}^2}{\varepsilon_2} a \ln\left(\frac{\mathrm{j}\gamma k_{\rho 2} a}{2}\right) - \frac{k_{\rho 1}}{\varepsilon_1}\frac{J_0(k_{\rho 1}a)}{J_1(k_{\rho 1}a)}}{\frac{2}{\varepsilon_2 a} - \frac{k_{\rho 1}}{\varepsilon_1}\frac{J_0(k_{\rho 1}a)}{J_1(k_{\rho 1}a)}} \frac{4\mathrm{j}}{\pi k_{\rho 2}^2 a^2} \approx \frac{-\frac{k_{\rho 2}^2}{\varepsilon_2} b \ln\left(\frac{\mathrm{j}\gamma k_{\rho 2} b}{2}\right) - \frac{k_{\rho 3}}{\varepsilon_3}\frac{H_0^{(2)}(k_{\rho 3}b)}{H_1^{(2)}(k_{\rho 3}b)}}{\frac{2}{\varepsilon_2 b} - \frac{k_{\rho 3}}{\varepsilon_3}\frac{H_0^{(2)}(k_{\rho 3}b)}{H_1^{(2)}(k_{\rho 3}b)}} \frac{4\mathrm{j}}{\pi k_{\rho 2}^2 b^2} \tag{2.56}$$

In (2.56)

$$\frac{2}{\varepsilon_2 a} >> \frac{k_{\rho 1}}{\varepsilon_1}\frac{J_0(k_{\rho 1}a)}{J_1(k_{\rho 1}a)} \tag{2.57}$$

and

$$\frac{2}{\varepsilon_2 b} >> \frac{k_{\rho 3}}{\varepsilon_3}\frac{H_0^{(2)}(k_{\rho 3}b)}{H_1^{(2)}(k_{\rho 3}b)} \tag{2.58}$$

and thus (2.56) can be approximated by

$$\left[-\frac{k_{\rho 2}^2}{\varepsilon_2} a \ln\left(\frac{\mathrm{j}\gamma k_{\rho 2} a}{2}\right) - \frac{k_{\rho 1}}{\varepsilon_1}\frac{J_0(k_{\rho 1}a)}{J_1(k_{\rho 1}a)}\right]\frac{1}{a} \approx \left[-\frac{k_{\rho 2}^2}{\varepsilon_2} b \ln\left(\frac{\mathrm{j}\gamma k_{\rho 2} b}{2}\right) - \frac{k_{\rho 3}}{\varepsilon_3}\frac{H_0^{(2)}(k_{\rho 3}b)}{H_1^{(2)}(k_{\rho 3}b)}\right]\frac{1}{b} \tag{2.59}$$

As k_1 and k_3 are much larger than k_z, additional approximations can be made for $k_{\rho 1}$ and $k_{\rho 3}$.

$$k_{\rho 1} = +\sqrt{k_1^2 - k_z^2} \tag{2.60}$$

$$\approx +\sqrt{k_1^2} \tag{2.61}$$

$$\approx k_1 \tag{2.62}$$

and likewise

$$k_{\rho 3} \approx k_3 \tag{2.63}$$

which allows the small argument equation to be written as

$$k_{\rho 2} \approx \left[\frac{\varepsilon_2}{\ln \frac{b}{a}} \left(\frac{k_1}{\varepsilon_1} \frac{1}{a} \frac{J_0(k_1 a)}{J_1(k_1 a)} - \frac{k_3}{\varepsilon_3} \frac{1}{b} \frac{H_0^{(2)}(k_3 b)}{H_1^{(2)}(k_3 b)} \right) \right]^{\frac{1}{2}} \tag{2.64}$$

Equation (2.64) provides an excellent initial value for the least squares routine, which typically only requires one iteration from this starting point.

2.6 Conclusion

In this chapter a full wave analysis of the quasi-TEM mode of a coaxial system was performed. The analysis used Hertzian vector potentials and the radial dependence was found to be described by the Bessel equation. Appropriate Bessel functions were chosen according to expected field behaviour in order to simplify the manipulations. Tangential electric and magnetic fields were matched at boundaries to create the wavenumber equations.

As a first step a wavenumber equation for the Sommerfeld mode was found and electric field lines compared to those reported by Sommerfeld and Stratton. It was found that the field lines compared well to Sommerfeld's lines while Stratton's lines were inconsistent.

To aid the numerical convergence for the quasi-TEM mode large and small argument approximations were used to provide a good starting position. With this starting position convergence was found to be very quick.

In Chapter 4 the calculated wavenumbers are compared to measurements of non-magnetic wires.

Chapter 3

The Measurement System

3.1 Introduction

The measurement system used in this thesis is a coaxial transmission line fed by an SMA connector on one end and terminated by a short circuit on the other. A diagram of the system is shown in Fig. 3.1. The centre conductor is the wire under test.

At first it was hoped that a system based on the Sommerfeld mode could be used. The equations describing the Sommerfeld mode are simple and relate the mode to the material properties of the wire. Thus the mode could be used to measure those properties. However, launching the Sommerfeld mode in a controlled way can be difficult as some radiation will occur [26, §III]. The Sommerfeld mode has a large (theoretically infinite) radial extent which means the environment around the experimental setup will have an effect. Also, as the system is open, it is possible that external radiation could interfere with the measurements.

Instead a coaxial system was chosen, with an outer conductor so large that its influence could be ignored. The closed coaxial system is immune to environmental effects and the quasi-TEM mode can be launched in a controlled way. However, the field equations describing the quasi-TEM mode are too complicated to be used directly. Perturbing the lossless TEM coaxial mode by the internal impedance of the wire provides an excellent approximate solution.

The SMA connector will carry energy in a TM mode (quasi-TEM—see §2.2) from the network analyser feed cable to the junction. The junction between the SMA feed and the coaxial cavity does not excite TE modes but instead gives rise to higher order evanescent TM modes. The energy in these modes can be represented by a shunt capacitance [19, p. 575].

Initially a double-sided coaxial measurement system with SMA connectors on both ends was created. This system allows for both S_{11} and S_{21} measurements. It

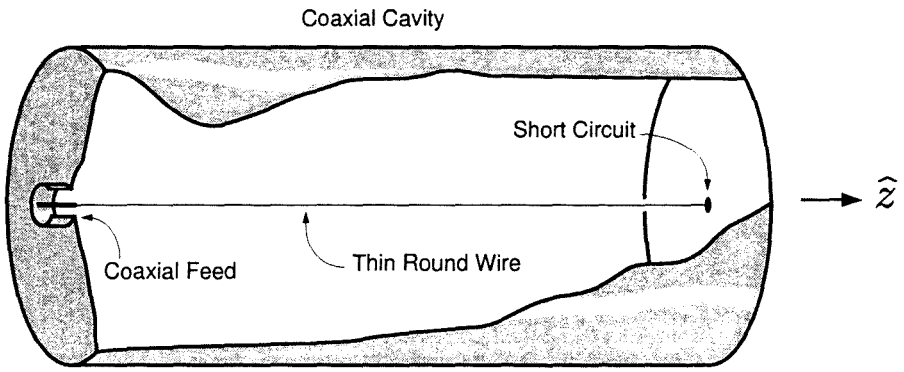

Figure 3.1: The coaxial cavity measurement system showing the good short circuit and the coaxial SMA feed. The centre conductor is the wire under test.

was hoped that the junction capacitance could be isolated and de-embedded in the frequency domain with this system. The de-embedding made use of the assumption that both feeds are identical, but small differences between the feeds created errors. At the same time the loading effect of a feed at each end prevented the use of short-circuited transmission line assumptions, used in the theory to find the wire surface impedance. Another disadvantage is that a full 2-port measurement requires longer cables and a full calibration.

Instead, a method for measuring the capacitance using time-gating on a 1-port measurement was developed. The SMA connector at one end was replaced by a good short circuit and the length of the system increased to provide enough time for the gate, as explained in §3.4.2. Only a 1-port calibration is required for these measurements, and a short phase-stable cable could be used to connect the system to the network analyser.

The SMA feed length and junction capacitance are removed from the non time-gated measurement in order to find the input impedance of the coaxial line at half-wavelength resonance. The input resistance and resonant frequency are related to the permeability, as shown in §3.3. The permeability is thus essentially found from a direct extraction method. Other methods were not investigated.

In the following sections the complex permeability is related to the surface impedance of the wire. A technique for measuring this impedance using half-wavelength resonance effects is developed.

A transmission line model of the system is created and each component of the model discussed. Special attention is paid to the time-domain gate which is used to find the feed junction capacitance.

A sensitivity analysis is performed and the system is found to be highly sensitive to length and resonance frequency accuracy. Methods for overcoming these

difficulties are proposed.

Finally a comparison is made between a measurement and prediction for the reflection coefficient of the system when a copper wire is present. The comparison demonstrates that the model is valid and accurate.

3.2 Physical Construction

The outer conductor of the coaxial cavity is an aluminium circular waveguide of 79.2 mm inner diameter. This diameter is 2 orders larger than the diameters of the wires under test. Hence the internal impedance of the outer conductor is negligible, as shown in §3.3.1.

Initially a pipe with a length just over 1 m was used, but this did not allow for the use of the desired time gate. A longer pipe was chosen and the inner length of the system was measured to be 1.58272 m to the accuracy of 10 μm at 21 °C using a computer controlled measurement system. This length provides approximately 10.6 ns between reflections from the short circuit, which is enough for the "maximum" time-gate shape over the band of interest (see §3.4.2). This gate has the lowest side-lobe levels and thus provides the best isolation of the reflection off the junction from subsequent reflections.

At each end the line is closed by aluminium end plates 2.9 mm thick. On the one end an SMA adapter feeds the signal to the centre wire. The wire is soldered to the SMA pin and stretched taut along the centre of the circular waveguide. On the other end it is pulled through the end plate and soldered into position. Initially a small spring was placed between the wire and the SMA pin to pull the wire taut. However, it was found that the inductance of the spring had a dominant effect on the measurements and it was removed.

A 4×4 cm observation hole is cut into the side of the circular waveguide at the short circuit end. This hole allows for soldering the wire, and is closed with a tight-fitting lid during the measurements.

The system was placed on its side during the measurements. This causes a small amount of sag of the inner wire. If the sag is too great the coaxial transmission line becomes non-linear and undesired modes are excited.

3.3 Measurement Theory

The system is treated as a low-loss transmission line with a short circuit termination. The resonances caused by this termination are used to measure the attenuation and electrical length of the line.

The attenuation is found when the length of the line is equal to a multiple of half a wavelength. At this frequency the short circuit at the load is transformed to the beginning of the line. However, instead of measuring zero input impedance, a finite resistance related to the attenuation is found. At the same time the wavelength must be a multiple of twice the physical length of the coaxial cavity, which provides the propagation constant.

The attenuation and propagation constants are related to the wire surface impedance using transmission line theory. The surface impedance is in turn related to the complex permeability using the skin effect.

3.3.1 Surface Impedance and Complex Permeability

The skin depth is found by solving Maxwell's equations for field penetration into a good conductor [19, p. 149]. Equation (2.14) can be written as

$$\nabla^2 \mathbf{E} = \tau^2 \mathbf{E} \tag{3.1}$$

where

$$\tau \triangleq (\mathrm{j}\omega\mu\sigma)^{\frac{1}{2}} \tag{3.2}$$

The solution of this equation for a plane wave propagating normal to a semi-infinite solid is useful as it can be applied by approximation to the coaxial system. It is solved for a good conductor filling the half-space $x > 0$. For an electric field in the $\hat{z}$ direction the field inside the conductor is

$$E_z = E_0 e^{-\tau x} \tag{3.3}$$

where the electric field at the surface $x = 0$ is E_0 and the surface current is related to this field by

$$J_0 = \sigma E_0 \tag{3.4}$$

Surface impedance is defined as

$$Z_s \triangleq \frac{E_0}{J_{sz}} = R_s + \mathrm{j}\omega L_s \tag{3.5}$$

where J_{sz} is the total $\hat{z}$ directed current in the half-plane:

$$J_{sz} = \int_0^\infty J_z dx \tag{3.6}$$

$$= \int_0^\infty J_0 e^{-\tau x} dx \tag{3.7}$$

$$= \frac{J_0}{\tau} \tag{3.8}$$

Thus the surface impedance can be written as

$$Z_s = \frac{\tau}{\sigma} \tag{3.9}$$

For complex $\mu = |\mu|e^{-j\delta_\mu}$, τ can be written as

$$\tau = \sqrt{\omega\sigma|\mu|}e^{j(\frac{\pi}{4}-\frac{\delta_\mu}{2})} \tag{3.10}$$

$$\Longrightarrow \Re\{\tau\} = \sqrt{\omega\sigma|\mu|}\cos(\frac{\pi}{4}-\frac{\delta_\mu}{2}) \tag{3.11}$$

$$\Im\{\tau\} = \sqrt{\omega\sigma|\mu|}\sin(\frac{\pi}{4}-\frac{\delta_\mu}{2}) \tag{3.12}$$

where $1/\Re\{\tau\}$ is the skin depth of the conductor, i.e. the depth at which the field strength is approximately 37% of its value at the surface.

The surface resistance and inductance are then

$$R_s = \sqrt{\frac{\omega|\mu|}{\sigma}}\cos(\frac{\pi}{4}-\frac{\delta_\mu}{2}) \tag{3.13}$$

$$L_s = \sqrt{\frac{|\mu|}{\omega\sigma}}\sin(\frac{\pi}{4}-\frac{\delta_\mu}{2}) \tag{3.14}$$

This solution is obtained for a semi-infinite solid, but can be applied to a good approximation to the thin round wires, as the depth of penetration is extremely small at frequencies above a few hundred kilohertz for a good conductor. Thus the wire is treated as a flat surface with a width equal to the circumference of the wire, and the resistance and internal inductance per-unit- length are given by

$$Z_i = R_i + j\omega L_i = \frac{1}{2\pi a} \times Z_s \tag{3.15}$$

where a is the radius of the wire. These values can be used in a transmission line model.

For example, if the inner wire is copper with a conductivity of 5.8×10^7 S/m and a diameter of 0.1 mm, $\mu_r = 1 + j0$ and the skin depth is approximately 2.1 μm at 1 GHz, 150 times smaller than the circumference of the wire. The internal impedance is $26.26 + j\omega 4.17 \times 10^{-9}\ \Omega/\text{m}$. For a steel wire with the same diameter but with a conductivity of 10^7 S/m and a relative permeability of $\mu_r = 10 - j10$ the skin depth is approximately 1 μm and the internal impedance is $310.73 + j\omega 20.5 \times 10^{-9}\ \Omega/\text{m}$.

The same approach can be taken for the outer conductor of the coaxial system. However, as the radius of the aluminium pipe is several orders larger than the thin wire, the internal impedance of the outer is several orders of magnitude smaller than the internal impedance of the wire and can be ignored. For example, at 1 GHz the internal impedance for this aluminium system with a radius of 39.6 mm is $0.414 + j\omega 6.59 \times 10^{-12}\ \Omega/\text{m}$.

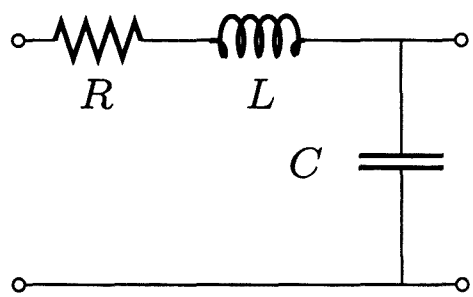

Figure 3.2: A unit cell of a transmission line. Shunt conductance is ignored for the air-filled coaxial system.

3.3.2 Internal Impedance and Low-Loss Transmission Line Theory

As the system is made from highly conducting materials, it can be modelled as a low-loss transmission line [19, p. 247]. A unit cell of the transmission line is shown in Fig. 3.2. There is no shunt conductance as the coaxial system is air filled and the properties of vacuum are assumed.

The per-unit-length parameters of the transmission line cell are well known for a lossless free space coaxial system as [19, pp. 26,83]

$$C = \frac{2\pi\varepsilon_0}{\ln\left(\frac{b}{a}\right)} \tag{3.16}$$

$$L_e = \frac{\mu_0}{2\pi}\ln\left(\frac{b}{a}\right) \tag{3.17}$$

$$R = 0 \tag{3.18}$$

where a is the inner wire radius and b is the outer radius. C is the per-unit-length capacitance and L_e is the per-unit-length external self-inductance of the system. R, the per-unit-length resistance, is zero, as the ideal line has no loss.

These lossless values can be perturbed by the internal impedance of the wire to obtain the approximate per-unit-length values because the system is low-loss:

$$L \approx L_e + L_i \tag{3.19}$$

$$R \approx R_i \tag{3.20}$$

where L_i is the per-unit-length internal inductance of the wire and R_i is its internal resistance. Thus the inductance consists of the external inductance of a lossless coaxial system and the internal inductance of the wire. The capacitance

is the same as for the lossless case and resistance is present because of the finite conductivity of the wire.

Low-loss transmission line approximations are based on the requirement that

$$\frac{R}{\omega L} \ll 1 \tag{3.21}$$

and this leads to approximations for the characteristic impedance and propagation constant.

The characteristic impedance of the line is

$$Z_c = \left(\frac{R+\mathrm{j}\omega L}{\mathrm{j}\omega C}\right)^{\frac{1}{2}} \tag{3.22}$$

$$= \sqrt{\frac{L}{C}}\left(1-\mathrm{j}\frac{R}{\omega L}\right)^{\frac{1}{2}} \tag{3.23}$$

The second term can be expanded using the binomial theorem to the first order as

$$Z_c \approx \sqrt{\frac{L}{C}}\left(1-\mathrm{j}\frac{R}{2\omega L}\right) \tag{3.24}$$

$$= R_c + \frac{1}{\mathrm{j}\omega C_c} \tag{3.25}$$

$$\Longrightarrow R_c = \sqrt{\frac{L}{C}} \tag{3.26}$$

$$\text{and } C_c = \frac{2L}{R\sqrt{L/C}} \tag{3.27}$$

Thus the low-loss transmission line characteristic impedance is complex and can be modelled as a resistor (R_c) in series with a capacitor (C_c).

The wavenumber $\gamma = \alpha + \mathrm{j}\beta$ is found from

$$\gamma = [(R+\mathrm{j}\omega L)(\mathrm{j}\omega C)]^{\frac{1}{2}} \tag{3.28}$$

$$= \mathrm{j}\omega\sqrt{LC}\left(1-\mathrm{j}\frac{R}{\omega L}\right)^{\frac{1}{2}} \tag{3.29}$$

A first order binomial expansion leads to

$$\alpha \approx \frac{R}{2\sqrt{L/C}} \tag{3.30}$$

$$\beta \approx \omega\sqrt{LC} \tag{3.31}$$

and with (3.19) and (3.20) the attenuation and phase constants become

$$\alpha \approx \frac{R_i}{2\sqrt{(L_e + L_i)/C}} \tag{3.32}$$

$$\beta \approx \omega\sqrt{(L_e + L_i)C} \tag{3.33}$$

For example, if the centre wire is copper with a diameter of 0.1 mm, the per-unit-length parameters are $C = 8.34\,\text{pF/m}$, $L_e = 1.335\,\mu\text{H/m}$ and at 1 GHz (using the internal impedance calculated in the previous paragraph) $L = L_e + L_i \approx 1.355\,\mu\text{H/m}$ and $R = R_i \approx 26.26\,\Omega\text{/m}$. Note that the internal inductance of the wire is several orders smaller than the external inductance.

The calculated values of the per-unit-length parameters can be used to test the low-loss approximation: $R/\omega L = 3.13 \times 10^{-3} \ll 1$ at 1 GHz. Thus the low-loss approximations are valid. The characteristic impedance is $Z_c \approx 403.1 - \text{j}0.631\,\Omega$ which shows that the real part of the characteristic impedance is much greater than the imaginary part. The attenuation constant for this example is $\alpha \approx 0.033\,\text{Np/m}$ and the phase constant $\beta \approx 21.12\,\text{rad/m}$.

3.3.3 Low-Loss Transmission Line at Half-Wavelength Resonance

The coaxial transmission line is terminated by a good short circuit. Thus a multiple of a half-wavelength away from the termination the voltage will be small and the current large. The line is near resonance and the electric and magnetic energies are almost equal, giving a small imaginary part of the input impedance. It is possible to take advantage of this effect to find α, β and the resonance frequency f_r in order to find the internal impedance of the wire.

At half-wavelength resonance the length of the line is related to the propagation constant by

$$\ell = \frac{\lambda}{2}n \tag{3.34}$$

$$\implies \beta = \frac{n\pi}{\ell} \tag{3.35}$$

where ℓ is the length of the line and n is an integer giving the multiple of the half-wavelength.

Substituting this phase constant into the equation for input impedance of a low-loss transmission line with a short circuit termination [19, Table 5.11a] gives

the input impedance at resonance as

$$Z_r \approx Z_c \frac{\alpha\ell \cos\beta\ell + \mathrm{j}\sin\beta\ell}{\cos\beta\ell + \mathrm{j}\alpha\ell\sin\beta\ell} \tag{3.36}$$

$$= Z_c\alpha\ell \tag{3.37}$$

$$\approx \alpha\ell R_c\left(1 + \frac{1}{\mathrm{j}\omega C_c}\right) \tag{3.38}$$

using (3.25).

The imaginary part of the resonance input impedance can be written as

$$\Im\{Z_r\} = -\alpha\ell R_c \frac{R}{2\omega L} \tag{3.39}$$

and is small as long as R_c is not too large because for a low-loss transmission line $\alpha\ell \ll 1$ and $R/\omega L \ll 1$. Thus the resonance frequencies at which $\beta = n\pi/\ell$ can be found by searching for the points at which imaginary part of Z_r becomes zero. The small error introduced by the finite reactance in (3.39) introduces errors of at most 100 kHz for the measurement system in this thesis, and the error decreases as frequency increases.

The internal inductance of the wire can then be found by re-arranging (3.33) as

$$L_i = \frac{1}{C}\left(\frac{\beta}{2\pi f_r}\right)^2 - L_e \tag{3.40}$$

and R_c is now known from (3.26) as

$$R_c = \sqrt{\frac{L_e + Li}{C}} \tag{3.41}$$

The attenuation constant α can be found from the real part of the resonance input impedance Z_r in (3.38) as

$$\alpha = \frac{R_r}{\ell R_c} \tag{3.42}$$

where $R_r = \Re\{Z_r\}$. This allows for the measurement of α which in turn is related to the internal resistance of the wire by inverting (3.32):

$$R_i = 2\alpha R_c \tag{3.43}$$

Thus the internal impedance of the wire as well as the resonance frequency can be measured for each multiple of a half-wavelength using this method.

3.3.4 Combined Complex Permeability, Low-Loss Transmission Line and Half-Wave Resonance Theory

The theory of the previous paragraphs is combined to relate μ directly to the two measured parameters, the resonance resistance R_r and the resonant frequency f_r. From the definition of τ in (3.2)

$$|\mu| = \frac{|\tau|^2}{2\pi f_r \sigma} \tag{3.44}$$

$$= \frac{\sigma}{2\pi f_r} |Z_s|^2 \tag{3.45}$$

$$= \frac{2\pi a^2 \sigma}{f_r} |R_i + \mathrm{j}2\pi f_r L_i|^2 \tag{3.46}$$

where (3.9) relates τ to the surface impedance, and the relation between surface impedance and internal impedance (3.15) has been used.

The internal inductance of the wire is known from (3.40) and internal resistance of the wire is related to α and the resonance resistance using (3.42) and (3.43) as

$$R_i = \frac{2R_r}{\ell} \tag{3.47}$$

Thus $|\mu|$ becomes

$$|\mu| = \frac{2\pi a^2 \sigma}{f_r} \left| \frac{2R_r}{\ell} + \mathrm{j}2\pi f_r \left(\frac{1}{C} \left(\frac{\beta}{2\pi f_r} \right)^2 - L_e \right) \right|^2 \tag{3.48}$$

$$= \frac{2\pi a^2 \sigma}{f_r} \left[\frac{4R_r^2}{\ell^2} + f_r^2 \ln^2(b/a) \left(\frac{n^2}{4\varepsilon_0 \ell^2 f_r^2} - \mu_0 \right)^2 \right] \tag{3.49}$$

where (3.30), (3.35) and the lossless C and L_e have been used. Similarly the angle of μ can be written as

$$\delta_\mu = \frac{\pi}{2} - 2 \arctan \left[\frac{\ell f_r \ln(b/a)}{2R_r} \left(\frac{n^2}{4\varepsilon_0 \ell^2 f_r^2} - \mu_0 \right) \right] \tag{3.50}$$

3.4 Model of the System

The complete system is modelled using transmission line and circuit theory. The SMA feed is treated as a short lossless transmission line. The junction is modelled by a frequency dependent shunt capacitance which is measured using time-domain gating. The coaxial cavity is treated as a low-loss transmission line with a short circuit termination. The model of the system is shown in Fig. 3.3.

The model consists of four sections:

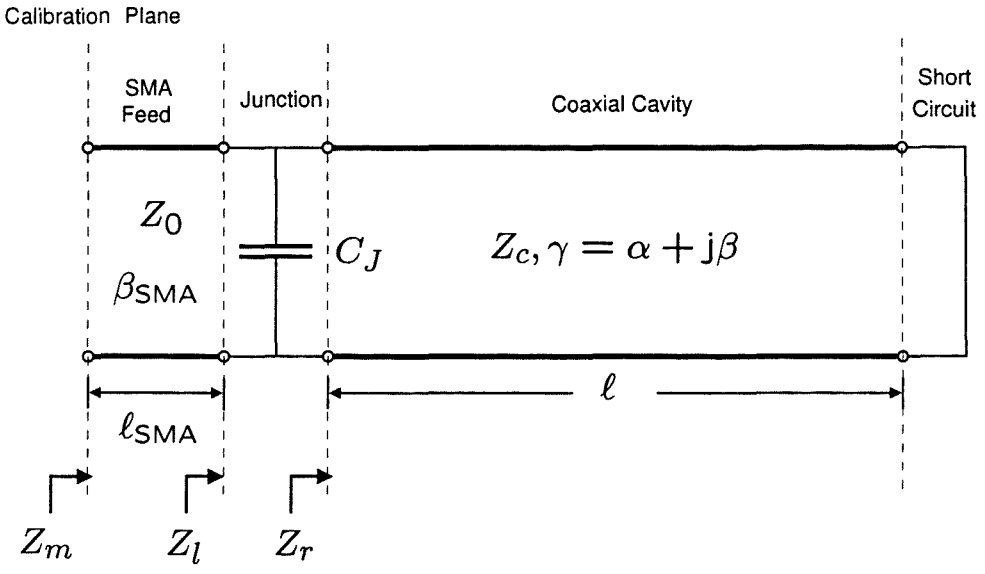

Figure 3.3: Model of the system showing the SMA feed, junction capacitance, coaxial cavity and good short circuit termination.

1. The SMA connector that feeds the cavity. This connector is treated as a lossless transmission line with a propagation constant set by the permittivity of polytetrafluoroethylene (PTFE).

2. The junction capacitance C_J. As the modes are TM, the evanescent modes generated at the junction interface store nett electric energy. This effect is modelled as a single capacitance.

3. The coaxial cavity. This cavity consists of an aluminium circular waveguide pipe with the wire of interest strung along the centre. The cavity is terminated with a good short circuit.

4. The short circuit. This is created by placing an aluminium plate at the end of the coaxial cavity.

The measured input impedance Z_m is found from an S_{11} measurement in a $50\,\Omega$ system using the equation

$$Z_m = 50\left(\frac{1+S_{11}}{1-S_{11}}\right) \tag{3.51}$$

3.4.1 SMA Connector Feed

The mode in the cavity is quasi-TEM and the same mode is found in coaxial cable. Thus a simple coaxial feed can be used to excite the cavity. The measurement is performed using a test set with coaxial connectors, allowing calibrated connections to the SMA feed of the cavity.

The feed is a female panel-mount SMA connector [27, p. 119] with a characteristic impedance Z_0 of $50\,\Omega$. The connector dielectric is extended through the 2.9 mm aluminium plate creating a total transmission line length of $\ell_{SMA} = 10.47\,\text{mm}$. The permittivity of PTFE was determined to be $\varepsilon_r = 2$ by calculating the required dielectric constant for a $50\,\Omega$ impedance given the SMA dimensions. If losses are ignored the propagation constant is

$$\beta_{\text{SMA}} = \frac{2\pi f}{c}\sqrt{\epsilon_r} \tag{3.52}$$

where c is the speed of light in a vacuum.

The impedance Z_l is found from transmission line theory as

$$Z_l = 50\frac{\text{j}50\sin(\beta_{\text{SMA}}\ell_{\text{SMA}}) - Z_m\cos(\beta_{\text{SMA}}\ell_{\text{SMA}})}{\text{j}Z_m\sin(\beta_{\text{SMA}}\ell_{\text{SMA}}) - 50\cos(\beta_{\text{SMA}}\ell_{\text{SMA}})} \tag{3.53}$$

3.4.2 Junction Capacitance

In order to determine the junction capacitance a time-gated measurement of the first reflection is made. The measurement is converted to the time domain on the network analyser using the time bandpass function. Fig. 3.4 shows the first 10 reflections from the short circuit termination at the end of the coaxial cavity.

The time gate is applied to the first reflection, thus isolating the reflection from the junction. In order to improve accuracy the "maximum" gate shape was used as it has the lowest sidelobe levels. The minimum time span for this gate is $22.4/f_{\text{span}}$ where f_{span} is the frequency span of the measurement [28]. For the 3 GHz span used in these measurements this is approximately 7.5 ns. The 1.58272 m pipe has a time between reflections of approximately 10.6 ns assuming the speed of light in a vacuum. Thus there is sufficient time between reflections to apply the maximum gate.

In order to prevent time aliasing interfering with the first pulse, the total time length must be large enough for the reflections in the system to become negligible. Energy is lost in the centre wire and into the $50\,\Omega$ feed. A simple analysis can be performed using a reflection diagram. Assuming a $400\,\Omega$ coaxial system (see the example in §3.3.2) and ignoring the junction capacitance, the magnitude of the n th peak after the first reflection is given in dB by

$$20\log_{10}\left(0.22\text{e}^{-2\alpha\ell n}(0.77)^{n-1}1.77\right) \tag{3.54}$$

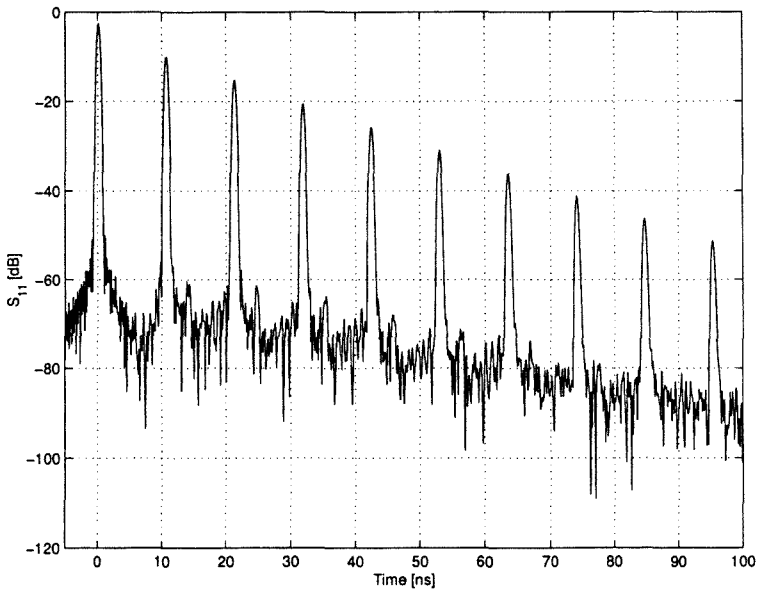

Figure 3.4: S_{11} measurement in the time domain showing the steadily diminishing reflections from the short circuit termination. The first peak is the reflection from the junction.

For $\alpha = 0.1\,\text{Np/m}$ and $\ell = 1.5\,\text{m}$, $n = 9$ gives approximately $-50\,\text{dB}$ which corresponds well with the 10 th peak on Fig. 3.4. In order to keep the reflection below $-80\,\text{dB}$ the equation gives $n > 15$. Thus the minimum time span must be greater than 160 ns, which gives a frequency step of at most 6.25 MHz in the frequency domain. The measurements made in this thesis have at least 801 points over a 3 GHz band, giving a maximum frequency step of approximately 3.75 MHz. Thus the frequency step is sufficient to prevent aliasing interference.

The gate is centred on the first peak and the span is set to 7.5 ns. The gate start and stop are then moved further away from the centre into the nearest nulls. Fig. 3.5 shows the time domain measurement with the gate applied. The maximum gate is inaccurate in the first and last 10% of the frequency band. However, a well applied gate can have small errors [28, p. 3.7–13].

The effect of isolating the first reflection is equivalent to having an infinitely long coaxial line, as there are no subsequent reflections. This is also the same as terminating the coaxial system in its own characteristic impedance. For a low-loss transmission line the characteristic impedance is complex as shown in (3.24), creating the equivalent circuit shown in Fig. 3.6. The load impedance Z_l is a capacitor in parallel with the characteristic impedance, which itself consists of a

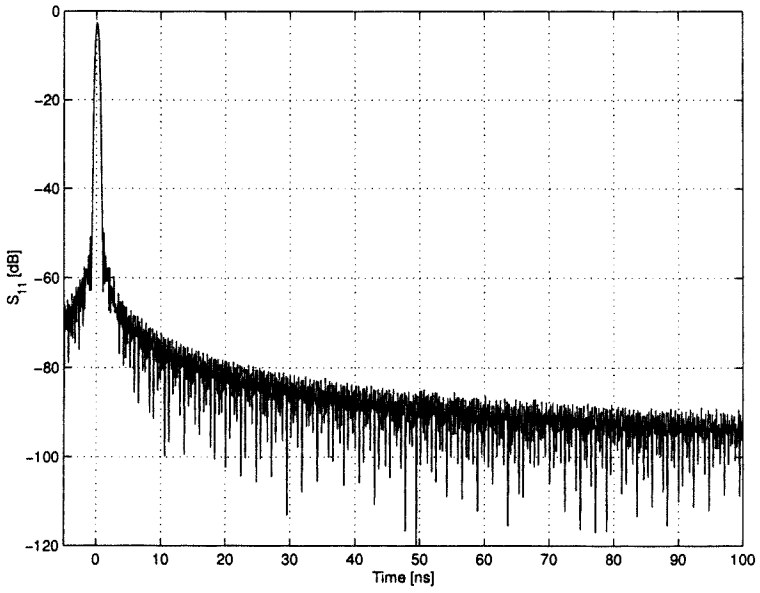

Figure 3.5: S_{11} measurement in the time domain with maximum gate applied. Only the reflection from the junction is present.

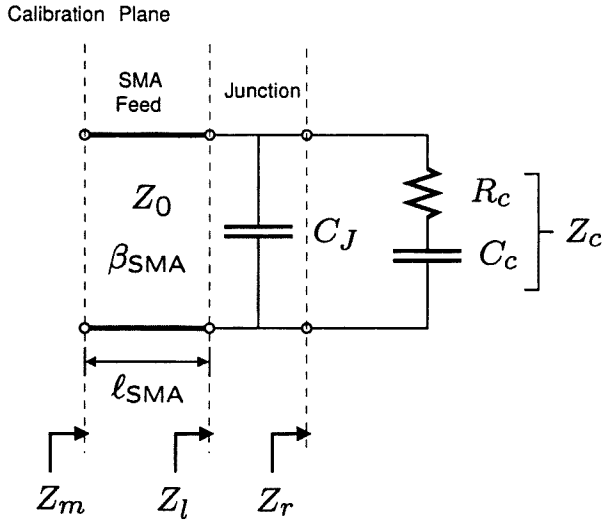

Figure 3.6: Equivalent circuit for the time-gated measurement.

resistor in series with a capacitor. The load admittance can be written as

$$Y_l = \mathrm{j}\omega\left(C_J + \frac{C_c}{1+\omega^2 C_c^2 R_c^2}\right) + \frac{\omega^2 C_c^2 R_c}{1+\omega^2 C_c^2 R_c^2} \tag{3.55}$$

From the low-loss approximations (3.26) and (3.27) R_c and C_c are known and

$$\omega^2 C_c^2 R_c^2 \approx \frac{4}{(R/\omega L)^2} \gg 1 \tag{3.56}$$

where for a low-loss system $R/\omega L \ll 1$. Thus the admittance can be written as

$$Y_l \approx \mathrm{j}\omega\left(C_J + \frac{R/\omega L}{2\omega R_c}\right) + 1/R_c \tag{3.57}$$

For the case where

$$C_J \gg \frac{R/\omega L}{2\omega R_c} \tag{3.58}$$

the load admittance becomes the simple case of the junction capacitance in parallel with a resistance. For example, if $R/\omega L \approx 0.01$, $R_c = 400\,\Omega$ and $f = 1\,\mathrm{GHz}$, $(R/\omega L)/(2\omega R_c) \approx 2 \times 10^{-15}$. For the coaxial system used in these measurements C_J has the order 10^{-13} so the condition is satisfied, and thus the junction capacitance can be found as

$$Y_l \approx \mathrm{j}\omega C_J + \frac{1}{R_c} \tag{3.59}$$

$$\Longrightarrow C_J \approx \frac{1}{\omega}\Im\{Y_l\} \tag{3.60}$$

$$\text{and } R_c \approx \frac{1}{\Re\{Y_l\}} \tag{3.61}$$

This measurement was made for all the wires and the junction capacitance was found to be approximately the same in each case. This suggests that the junction capacitance is dominantly a function of the outer coaxial step for the measurement system in this thesis.

The expected junction capacitance can be calculated using formulas from Marcuvitz [29, p. 310]. The approach requires several approximations. The junction is treated as a step in the outer radius of the coaxial system only. The dielectric of the SMA connector is ignored and the radius of the centre (or inner) conductor is kept constant at 0.64 mm (the SMA inner radius). Because the ratio between the radius of the outer conductor of the SMA connector (2.05 mm) and the radius of the outer conductor of the coaxial system (39.6 mm) is large there is a loss of accuracy. The distance between inner and outer of the SMA connector is

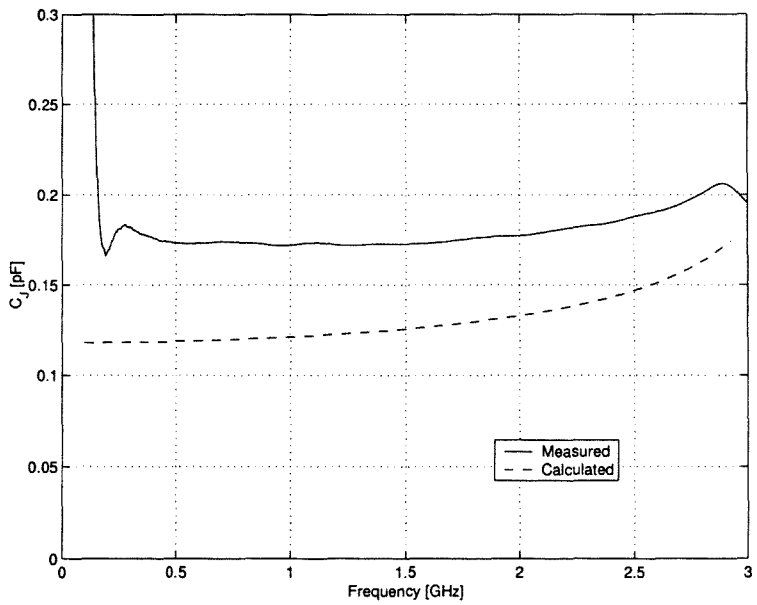

Figure 3.7: Measured junction capacitance for 0.26 mm non-magnetic wire with conductivity 1.6×10^6 S/m (see §4.2) compared to calculation of the single-step junction.

much smaller than the same distance for the coaxial system, which allows a small aperture approximation to be made.

Fig. 3.7 shows an example of the measured junction capacitance compared to calculated values, found from a measurement of the unknown non-magnetic wire (see §4.2). The maximum difference is approximately 0.06 pF or 30%. This is acceptable considering the approximations required. Note that the first and last 300 MHz of the measurement are considered inaccurate because of gating errors.

In Fig. 3.8 the measured and calculated characteristic impedances are compared for the same wire. The largest error is 1.3% at 1.94 GHz.

3.4.3 Coaxial Cavity

The transmission model of the coaxial cavity implicitly assumes that only the quasi-TEM mode is propagating. As frequency in the cavity is increased, other modes cut in. Because the feed is a TM mode and the junction is rotationally symmetrical these modes will also be TM. The upper frequency limit of the measurement system is thus set by the cutoff wavelength of the first TM mode according

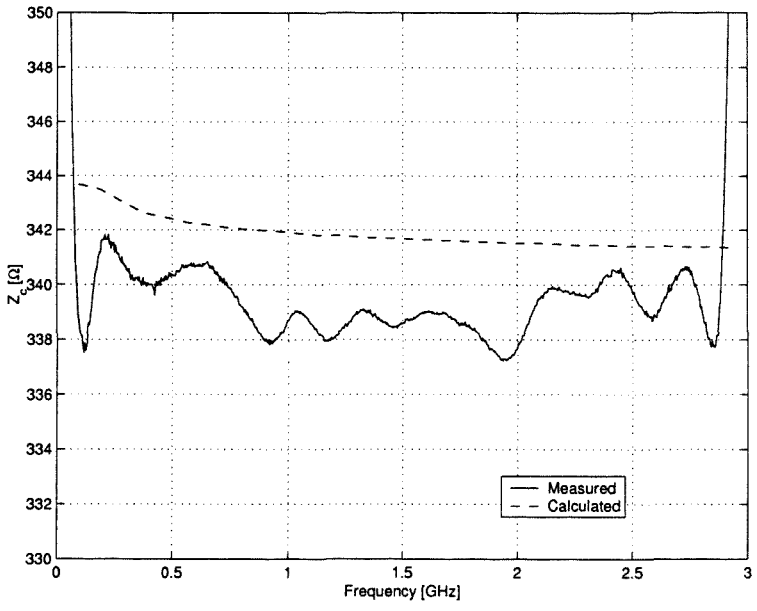

Figure 3.8: Measured and calculated real part of characteristic impedance for 0.26 mm non-magnetic wire with conductivity 1.6×10^6 S/m (see §4.2).

to the approximate equation [19, p. 435]

$$\lambda_c \approx \frac{2}{p}(b-a) \tag{3.62}$$

for the pth TM mode. For the system used in these measurements this frequency is approximately 3.8 GHz for $p = 1$. This is well above the maximum frequency used in these measurements.

The coaxial cavity input impedance Z_r (see Fig. 3.3) is found by taking the non time-gated S_{11} measurement and subtracting the junction capacitance from Z_l. This impedance shows sharp peaks at every uneven multiple of a quarter-wavelength and troughs at every half-wavelength resonance. Fig. 3.9 and 3.10 show the real and imaginary parts of the resonant cavity input impedance.

From the measured input impedance two values must be found: the input resistance at half-wavelength resonance and the corresponding half-wavelength resonance frequency. The input resistance at the half-wavelength resonance points is found by taking the minimum of each trough, as shown in Fig. 3.11. The resonance frequency is the corresponding frequency point. However, in order to improve accuracy an interpolation is necessary as shown in §3.5.

Surface roughness of the inner wire can be taken into account using a complex surface displacement [7, p. 55] but in this work the wires are considered to be

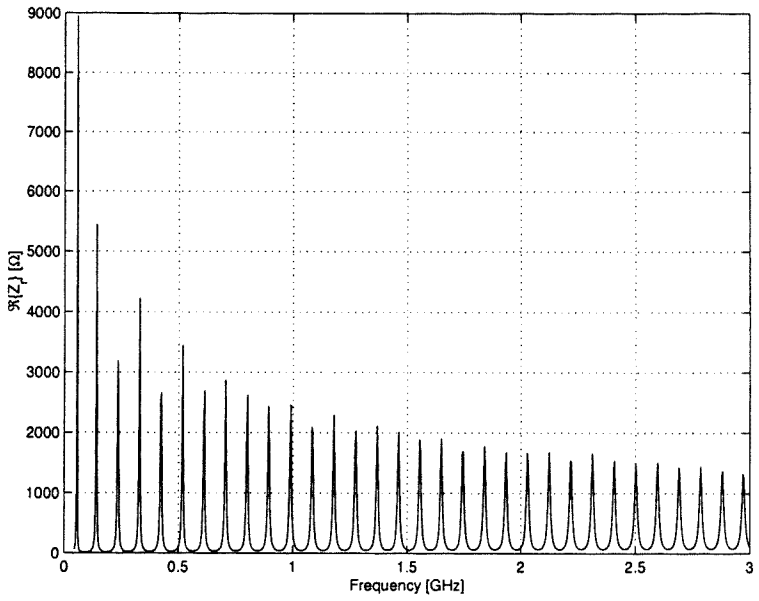

Figure 3.9: Real part of the resonant cavity input impedance.

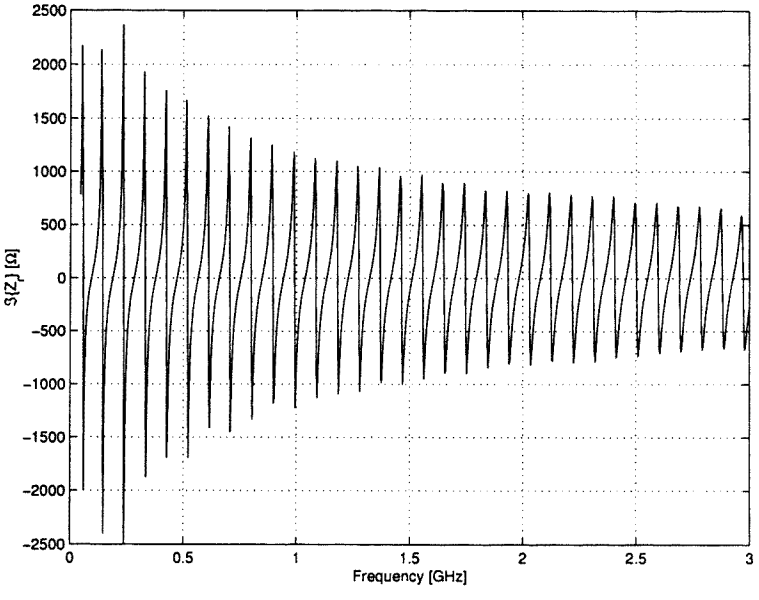

Figure 3.10: Imaginary part of the resonant cavity input impedance.

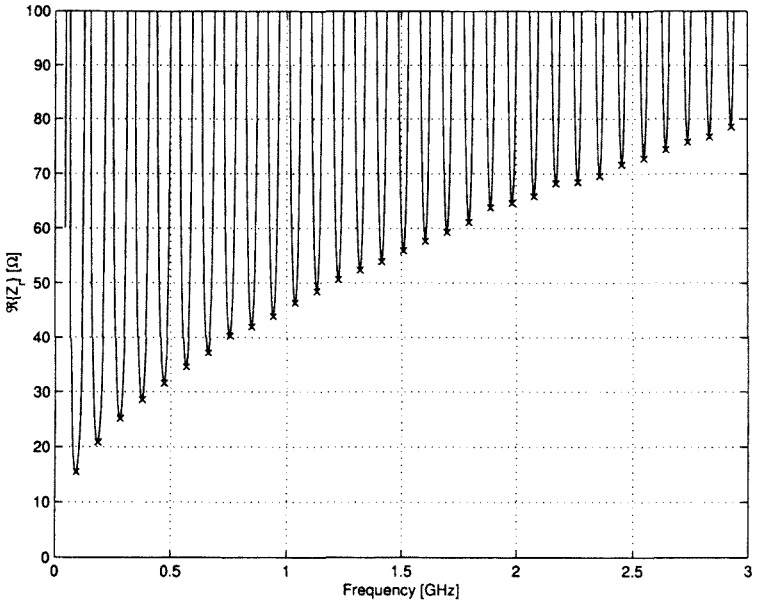

Figure 3.11: Input resistance at the half-wavelength resonance frequencies marked with x. As expected this non-magnetic wire has a $\sqrt{f}$ dependency associated with skin effect.

smooth. The effect of surface roughness on the inner wire of a coaxial line is to increase attenuation and make the transmission line parameters functions of frequency, while adding a delay-line effect at low frequencies. These effects were not observed during the measurements of the non-magnetic wires (see for example Fig. 4.2 and Fig. 4.6) indicating that they do not play a significant role.

3.4.4 The Short Circuit Termination

The short circuit can also be described using surface impedance. An analysis of this for the field distribution in a coaxial guide shows that the surface impedance is the same as for the plane wave case examined in §3.3.1. If the electric field is given by

$$\mathbf{E} = \hat{\rho}\frac{1}{\rho}E(z) \tag{3.63}$$

then (3.1) gives

$$\nabla^2\mathbf{E} = \tau^2\mathbf{E} \tag{3.64}$$

$$\implies \frac{1}{\rho}\frac{\partial}{\partial\rho}\left(\rho\frac{\partial}{\partial\rho}\left(\frac{E}{\rho}\right)\right) + \frac{\partial^2}{\partial z^2}\frac{E}{\rho} - \frac{1}{\rho^2}\frac{E}{\rho} = \tau^2\frac{E}{\rho} \tag{3.65}$$

$$\implies \frac{E}{\rho^3} + \frac{1}{\rho}\frac{\partial^2 E}{\partial z^2} - \frac{E}{\rho^3} = \tau^2\frac{E}{\rho} \tag{3.66}$$

$$\implies \frac{\mathrm{d}^2 E}{\mathrm{d}z^2} = \tau^2 E \tag{3.67}$$

which leads to the same surface impedance as for a plane wave incident on a conductive semi-infinite solid.

The end-plate is made of aluminium with a surface resistivity of $3.26\times10^{-7}\sqrt{f}$ Ω [19, p. 154]. At 3 GHz, the highest frequency used in the measurements, this resistivity is 10.31 mΩ. This is three orders of magnitude smaller than the surface resistance of the wire and can thus be ignored.

The surface inductance makes the coaxial system electrically longer. At 3 GHz the normalised reactance for a 400 Ω line is approximately $2.6 \times 10^{-5}\,\Omega$ which gives a length of less than 1 μm for a phase velocity of free space. This can safely be ignored.

The short circuit is thus shown to be close to ideal and can be taken as such.

3.5 Sensitivity Analysis

In order to improve the accuracy of the measurements it is vital to know which parameters have the largest effect on μ. A sensitivity analysis on $|\mu|$ is performed for this purpose. The sensitivity of $\angle\mu$ can be found using the same method and proves to be most sensitive to the same parameters as $|\mu|$.

The magnitude of μ can be written as

$$|\mu| = \frac{2\pi a^2\sigma}{f_r}\left[\frac{4R_r^2}{\ell^2} + f_r^2\ln^2(b/a)\left(\frac{n^2}{4\varepsilon_0\ell^2 f_r^2} - \mu_0\right)^2\right] \tag{3.68}$$

where f_r is the resonant frequency, a is the wire radius, R_r is the measured resistance at half-wavelength resonance and ℓ is the length of the coaxial system.

In order to find critical parameters a first-order sensitivity analysis is performed [30, p. 172]. The sensitivity of the magnitude of μ to parameter x is given by

$$S_x^{|\mu|} = \frac{x}{|\mu|}\frac{\partial|\mu|}{\partial x} \approx \frac{\frac{\Delta|\mu|}{|\mu|}}{\frac{\Delta x}{x}} \tag{3.69}$$

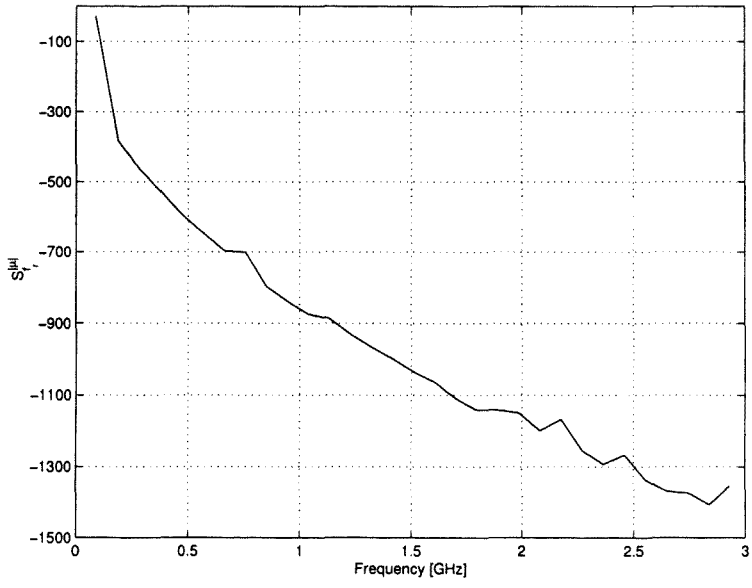

Figure 3.12: Sensitivity of $|\mu|$ of copper wire to resonant frequency.

The derivative of $|\mu|$ with respect to the various parameters can be taken analytically. The sensitivities to f_r, ℓ, a and R_r are shown in the following figures for a copper wire. The measurement of $|\mu|$ is most sensitive for the copper wire as copper has the highest conductivity of the wires used, and the sensitivities are proportional to σ, as can be seen from (3.68). It is clear from the sensitivity graphs that the most critical parameters are f_r and ℓ.

3.5.1 Sensitivity of $|\mu|$ to Resonant Frequency

At 3 GHz the f_r sensitivity is approximately -1400. With 801 points over a 3 GHz band the frequency step is approximately 3.75 MHz and the largest possible error is thus 1.875 MHz. This gives a $|\mu|$ error of 87.5% at 3 GHz using (3.69). An interpolation is necessary in order to improve the frequency resolution.

A half-wavelength resonant transmission line with a short circuit termination can be modelled as a series RCL circuit in the vicinity of resonance [31, p. 214]. The input reactance is

$$X_{\text{in}} = \omega_0 L \left(\frac{\omega}{\omega_0} - \frac{\omega_0}{\omega} \right) \tag{3.70}$$

where $\omega_0^2 = 1/LC$. Close to resonance the frequency can be written as $\omega = \omega_0 + \delta\omega$ with $\delta\omega$ small, and the reactance can be expanded using a first order

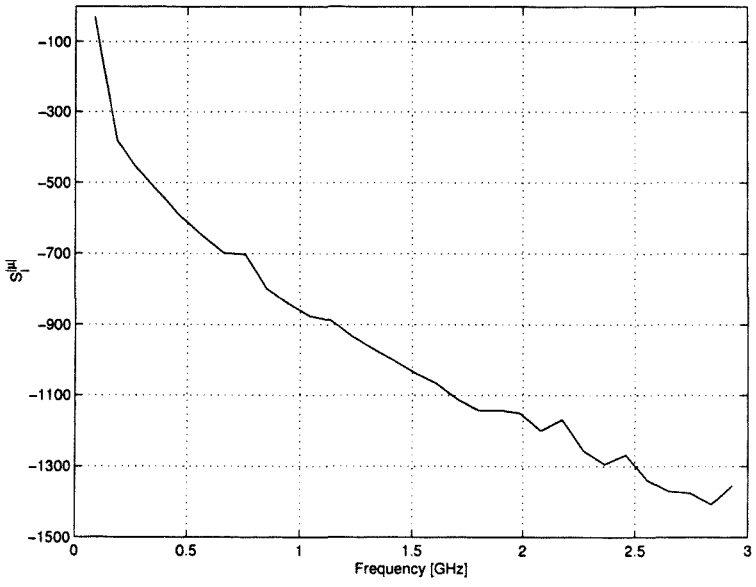

Figure 3.13: Sensitivity of $|\mu|$ of copper wire to length.

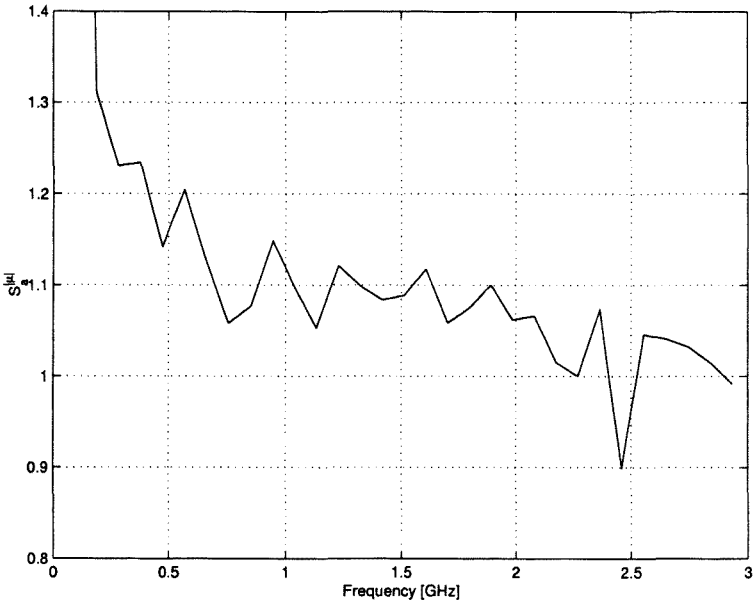

Figure 3.14: Sensitivity of $|\mu|$ of copper wire to wire radius.

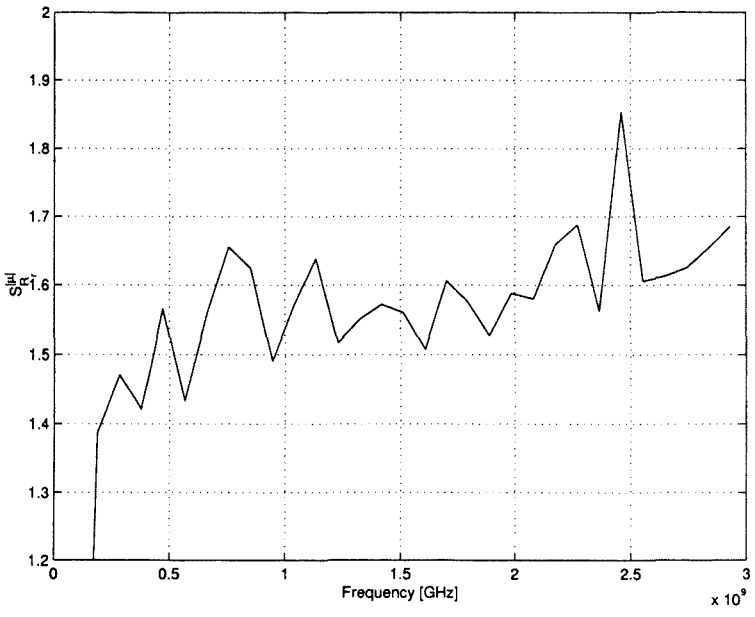

Figure 3.15: Sensitivity of $|\mu|$ of copper wire to resonance resistance.

binomial approximation as

$$X_{\text{in}} \approx 2L\delta\omega \tag{3.71}$$

Thus close to resonance the input reactance is approximately linear with frequency.

Thus a linear fit is made to a point on either side of the initial resonance frequency of the measured input reactance and the zero of this straight line is used as the interpolated resonance frequency.

3.5.2 Sensitivity of $|\mu|$ to Length

The sensitivity of $|\mu|$ to length requires that the length of coaxial line be known to an accuracy of 1.5 m/1400/10 $\approx$ 0.1 mm for a 10% accuracy of $|\mu|$ at 3 GHz. Although the length was measured to be 1.58272 m with a 10 μm accuracy, the high sensitivity implies that temperature effects play a role as the linear expansion coefficient of aluminium is 24×10^{-6} per degree centigrade [32, p. 514]. For a 5° change in temperature the length of the 1.5 m pipe changes by 0.18 mm which gives an 18% change in $|\mu|$ at 3 GHz.

A second important factor affecting the electrical length of the coaxial line is the permittivity of air. For dry air at room temperature a typical value for ε_r is 1.0006 [33, p. 2.44]. Over a distance of 1.58272 m this creates an electrical length

change of 0.475 mm. The exact value of ε_r depends on air pressure and humidity.

The measurements made in this thesis were not temperature or humidity controlled which creates a band of uncertainty. In Chapter 4 these uncertainties are included on the results graphs using error bars. Determination of the temperature and humidity would decrease the uncertainties associated with the measurement, but due to unavailability of equipment this was not done.

However, this problem can be avoided by using a non-magnetic wire as a standard and tuning the length parameter until a relative permeability of 1 is found. The non-magnetic wire is then replaced by the wire of interest and its permeability can be measured with a known effective length. This possibility was not exploited in this thesis as the intention was to make independent non-magnetic and magnetic measurements while proving the system.

3.6 D.C. Measurement of Conductivity

The ratio of $|\mu|$ to σ appears in the equations describing the relationship between permeability and surface impedance. In order to distinguish between them a separate measurement must be made. If surface roughness is neglected, the conductivity at high frequencies can be assumed to be the same as the bulk D.C. conductivity as can be seen from the Drude model [34, p. 288].

In order to measure the D.C. conductivity a resistor was measured on a calibrated HP8753 network analyser at 300 kHz. The use of the calibration standards introduces a traceable external reference. The resistance was measured as 1.19 Ω.

The calibrated resistor was then connected in series with the wire of interest to a D.C. supply in order to make a resistance measurement using an oscilloscope. The ratio of voltage drop to current over the wire gives the wire resistance at D.C. Oscilloscope errors give an uncertainty of approximately 2.5% for these measurements.

The conductivity of the wire is found from the analysis of a one-dimensional resistor with uniform conductivity [35, Ex. 7.2.1] as

$$\sigma = \frac{l}{RA} \tag{3.72}$$

where R is the measured resistance, l is the length of the wire and A its cross-sectional area. This value is compared to measurements made at high frequencies for the non-magnetic wires in Chapter 4.

3.7 Network Analyser Calibration and Use

For these high accuracy measurements care was taken to avoid introducing errors. An HP8510 network analyser was used. It was calibrated using an HP85053B economy calibration kit which consists of open, short and fixed load standards. It was not necessary to use a sliding load as the reflections from the system are strong and the measurements would not benefit from improved dynamic range.

A half-metre length of HP8210 phase stable cable with APC–7 to 3.5 mm converters was used to connect the network analyser to the measurement system. The cable was moved as little as possible during the calibration and final attachment. A male 3.5 mm connector was attached to a female SMA feed on the measurement system. This avoids the damage that would occur to the connectors if their sexes were swapped.

All of the connectors were cleaned using alcohol swabs and toothpicks and left to dry before being attached. A visual inspection of all the connecting surfaces was performed to check for scratches and other damage. The connections were made using the provided wrench that breaks at the correct torque, while the other connector was held firm with a spanner.

The network analyser was set to step mode to ensure a phase lock at each measurement frequency. Although this slows down the measurement it ensures that the phase measurement is accurate, especially for this low-loss resonant system where transient effects take some time to die down. Averaging was not used in these measurements.

The quality of the calibration was checked by re-attaching the short standard directly after calibration. The delay time was measured using the electrical delay function and compared to the delay in the standard's definition. This was consistently found to be within 0.6% suggesting that a good calibration had been made.

Two measurements were then made, one with a time gate placed around the first reflection and one without any gating. The data files were stored on a computer and Matlab was used to extract the complex permeability.

3.8 Comparison Between Measurement and Model

The complete transmission line model with calculated junction capacitance is compared to a reflection coefficient measurement in this section in order to confirm the accuracy of the model. Copper wire with a diameter of 140 μm is used, as the internal impedance of the wire can be calculated for a non-magnetic wire. The length of the line was taken as 1.58272 m and the line was assumed to be air filled. The conductivity of the copper was taken as 5.8×10^7 S/m [19, Table 3.17a].

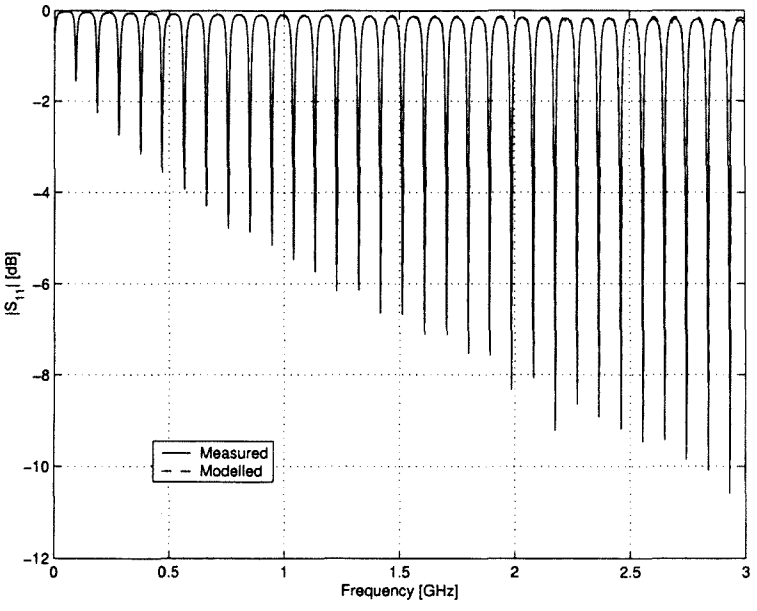

Figure 3.16: Magnitude comparison between the low-loss transmission line model and measured reflection coefficient for a copper wire (140 μm diameter, $\sigma = 5.8 \times 10^7$ S/m)

The comparison is shown in Fig. 3.16 for the magnitude and Fig. 3.17 for the angle of the reflection coefficient.

The model and the measurement match extremely well in both magnitude and phase. There is some shifting of the nulls at higher frequencies causing an 8° phase difference, and the peak magnitude is also 0.05 dB higher for the model at these frequencies. This indicates that the conductivity of the wire is lower than the pure copper value used, confirmed by the measurement results in §4.1.

The reflection coefficient is close to 1 which lowers the sensitivity of the measurements. However it should be noted that the half-wavelength resonance points of interest (where the input resistance R_r is extracted) correspond to the nulls of the reflection coefficient and are thus -2 dB or lower over the band of interest, avoiding the sensitivity problem.

Thus it is shown that the low-loss transmission line model of the measurements is valid and can provide accurate results.

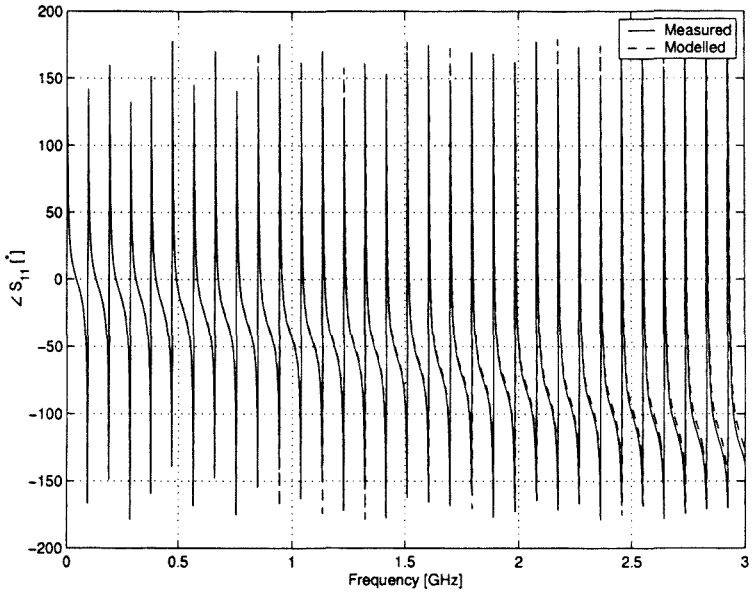

Figure 3.17: Angle comparison between the low-loss transmission line model and measured reflection coefficient for a copper wire (140 μm diameter, $\sigma = 5.8 \times 10^7$ S/m)

3.9 Conclusion

In this chapter complex permeability was related to surface impedance and in turn to the phase and attenuation constants of a low-loss coaxial system. These constants were then shown to be measurable using half-wavelength resonance effects.

A transmission line and circuit model of the system was created. It takes into account the phase change introduced by the SMA feed connector. Time gating, which effectively allowed for investigation into the reflection from the junction alone, was used to measure the junction capacitance so that its effect could be removed. Surface impedance concepts were used to show that the short circuit termination was close to ideal.

A sensitivity analysis was performed to highlight the key factors upon which μ depends. It was found that μ is extremely sensitive to resonant frequency and length. An interpolation was used to improve the frequency resolution. However, the length was found to have significant changes with temperature and humidity. As the measurements were not taken under controlled conditions these create uncertainties around the measurement results.

A carefully calibrated HP8510 network analyser was used to make the measurements. Phase stable cable was used to connect the measurement system to the

network analyser.

The predicted reflection coefficient of the complete low-loss transmission line model was compared to measurements and the model was found to be valid and to give good results.

Chapter 4

Measurement Results

In this chapter the measurement system is used to determine the permeability of three wires. The wires are listed in Table 4.1. The phase and attenuation constants for each wire are measured and μ is calculated.

The complex permeability $\mu = |\mu|e^{-\delta_\mu} = \mu_0(\mu_r' - j\mu_r'')$ is calculated from

$$|\mu| = \frac{2\pi a^2\sigma}{f_r}\left[\frac{4R_r^2}{\ell^2} + f_r^2\ln^2(b/a)\left(\frac{n^2}{4\varepsilon_0\varepsilon_r\ell^2 f_r^2} - \mu_0\right)^2\right] \quad (4.1)$$

$$\text{and } \delta_\mu = \frac{\pi}{2} - 2\arctan\left[\frac{\ell f_r\ln(b/a)}{2R_r}\left(\frac{n^2}{4\varepsilon_0\varepsilon_r\ell^2 f_r^2} - \mu_0\right)\right] \quad (4.2)$$

where the parameters are listed in Table 4.2.

In order to separate μ from σ a separate D.C. conductivity measurement is required, as described in §3.6. For non-magnetic wires μ is known and the conductivity measured at radio frequencies can be calculated as

$$\sigma = \frac{\pi f_r\mu_0\ell^2}{(4\pi aR_r)^2} \quad (4.3)$$

Table 4.1: The properties of the three measured wires.

Wire	Diameter	D.C. Conductivity	Magnetic
Copper	140 μm	5.46×10^7 S/m	No
Unknown	260 μm	1.72×10^6 S/m	No
Steel	330 μm	4.17×10^6 S/m	Yes

Table 4.2: The definitions of the parameters used to calculate μ.

Parameter	Definition
a	Inner wire radius
b	Coaxial outer conductor radius
ℓ	Coaxial pipe length
σ	D.C. conductivity of the wire
ε_r	Relative permittivity of the air
f_r	Resonant frequency
R_r	Measured input resistance at resonance
n	Half-wavelength multiple
ε_0	Permittivity of free space
μ_0	Permeability of free space

and compared to the D.C. measured value. The D.C. value is considered more reliable as it is less demanding both in terms of equipment and complexity.

For each wire the phase constant β and the attenuation constant α are shown. For the non-magnetic wires the constants are compared to calculated values found from the theory in Chapter 2. The measured D.C. conductivity values were used for the calculations. The axial wavenumber k_z from the theory chapter equation (2.15) is related to the wavenumber $\gamma = \alpha + \mathrm{j}\beta$ by $\gamma = \mathrm{j}k_z$.

α is closely related to the surface resistance and thus has approximately a $\sqrt{f}$ dependency. β is plotted as $\beta - \beta_0$ where β_0 is the propagation constant in free space. For a low-loss transmission line this can be written as

$$\beta - \beta_0 = \omega\sqrt{(L_e + L_i)C} - \omega\sqrt{L_eC} \tag{4.4}$$

$$= \omega\sqrt{L_eC}\left[\left(1 + \frac{L_i}{L_e}\right)^{\frac{1}{2}} - 1\right] \tag{4.5}$$

$$\approx \pi\sqrt{\frac{C}{L_e}} f L_i \tag{4.6}$$

using a first-order binomial expansion of the square root term in the brackets. L_i has a $1/\sqrt{f}$ dependency for non-magnetic wire and thus $\beta - \beta_0$ also has approxi-

Table 4.3: Uncertainties of the various parameters used to calculate μ.

Parameter	Variation	Cause of uncertainty
Δa	2.5 μm	Digital vernier
Δb	0.01 mm	5° temperature change
$\Delta \ell$	0.2 mm	5° temperature change
$\Delta \sigma$	2.5% of D.C. value	Oscilloscope errors
ΔR_r	50 mΩ	0.01 dB network analyser S_{11} error
$\Delta \varepsilon_r$	2×10^{-4}	Water vapour pressure of 30 mbar [36]
Δf_r	100 kHz	Non-zero imaginary resonance impedance

mately a $\sqrt{f}$ dependency in this case.

In order to show the effect of the various uncertainties of the system each parameter was set to its realistic extremes and μ calculated. These uncertainties are listed in Table 4.3. The effect of these extremes on μ_r' and μ_r'' is shown using error bars.

4.1 Copper Wire

Electrical grade copper wire with a plastic coating was used. The coating was burned off using a low temperature gas flame. The diameter of the wire was measured using a digital vernier as 140 μm and the D.C. conductivity was measured as $\sigma = 5.46 \times 10^7$ S/m. This is 6% lower than expected for copper (pure copper has $\sigma = 5.8\times10^7$ at 300 K [19, p. 154]) and indicates that the diameter of the wire may be smaller that 140 μm (the digital vernier only shows two decimal places and is thus subject to rounding errors) and that the copper may have low purity.

The measured conductivity at high frequencies is compared to the D.C. measurement in Fig. 4.1. The drop of the least-squares fit with frequency indicates that there is some error in the electrical length of the system. The difference between the least-squares fit and the D.C. measurement is 6% at the lowest frequency. The large variations at certain frequencies are as a result of the resonances found in α, discussed in the next paragraphs.

The measured and calculated attenuation constants α are compared in Fig. 4.2.

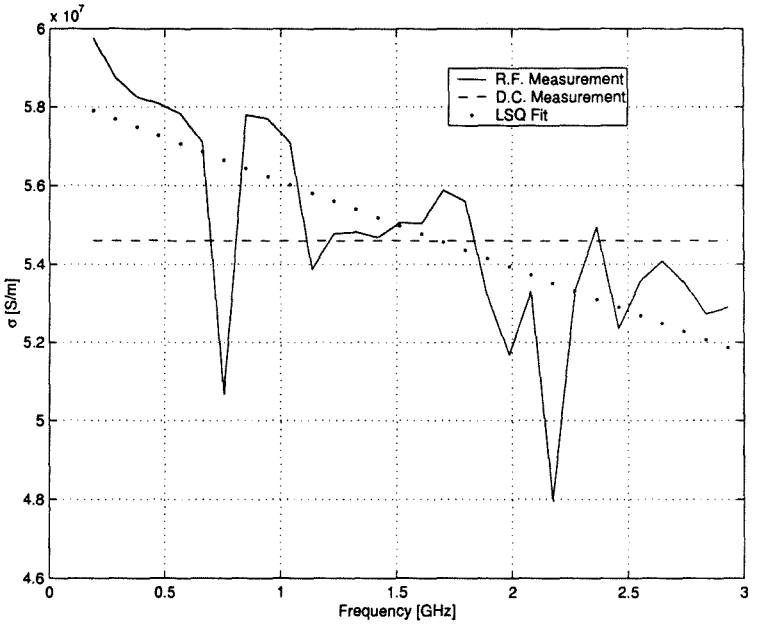

Figure 4.1: Conductivity of the copper wire comparing the R.F. measurement, with a least-squares fit, to the D.C. measurement.

The trends of the measurement and calculation are close to a $\sqrt{f}$ dependency as expected. The largest error in α is 8% at the lowest frequency. The $\sqrt{f}$ form of the measurement indicates that surface roughness does not play a role, as attenuation from surface roughness increases at a higher rate.

α shows two resonance peaks at 756 MHz and 2.175 GHz. These peaks are unexpected and re-occur in subsequent measurements (see Fig. 4.6). It is possible that the resonance at 2.175 GHz is related to the cut-off frequency of the TE_{10} mode [19, p. 435]. Numerically solving the characteristic equation for this mode gives a cut-off frequency of 2.2184 GHz which is within 50 MHz of the measurement. As the frequency domain is sampled approximately only every 100 MHz they may well correspond. The TE_{10} mode could be excited by wire sag, as the measurement system is placed on its side. The origin of the resonance at 756 MHz is unknown. However, the effect of both these peaks on μ is insignificant and they can safely be ignored.

The calculated phase constant β is compared to the measured value in Fig. 4.3. As expected, the $\beta - \beta_0$ graphs show a $\sqrt{f}$ dependency. The error increases with frequency to 31% at 3 GHz. β is highly dependent on length, and the large error suggests that the temperature and humidity variations are playing a role.

The relative permeability of the copper wire is shown in Fig. 4.4. The expected

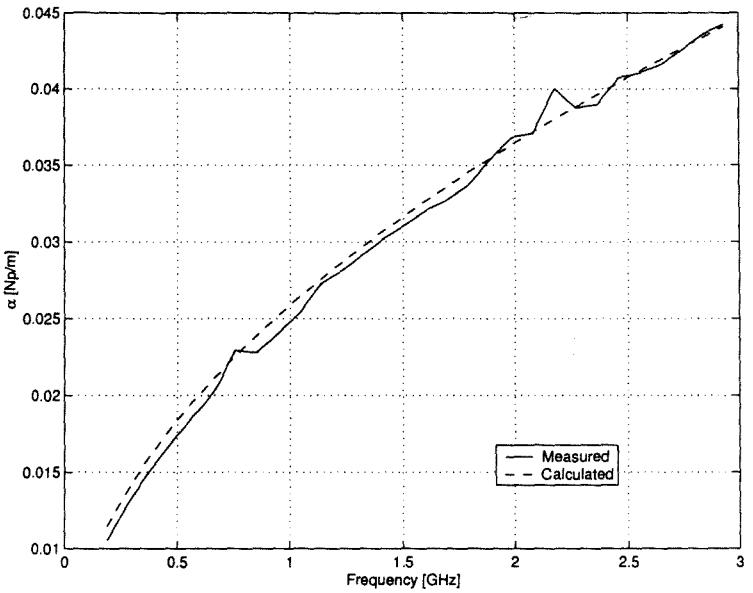

Figure 4.2: Comparison between measured and calculated α of the copper wire ($\sigma = 5.36 \times 10^7$ S/m).

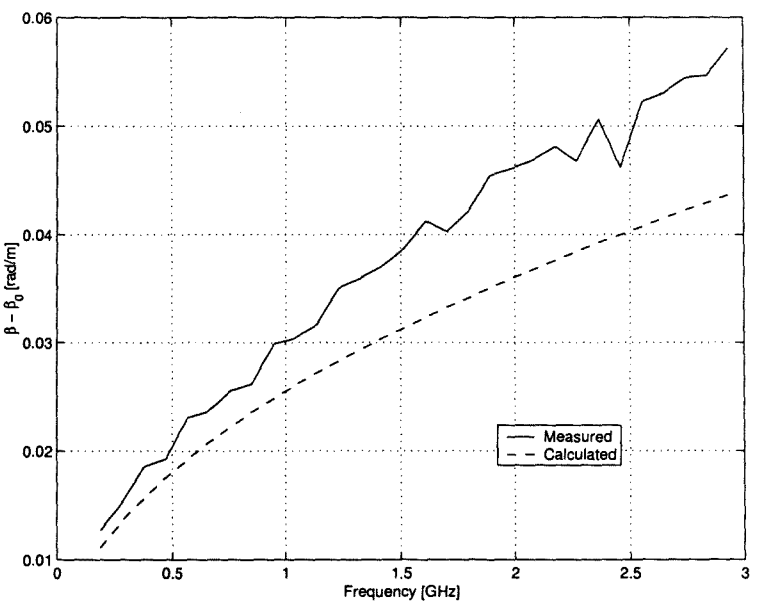

Figure 4.3: Comparison between measured and calculated β of the copper wire ($\sigma = 5.36 \times 10^7$ S/m).

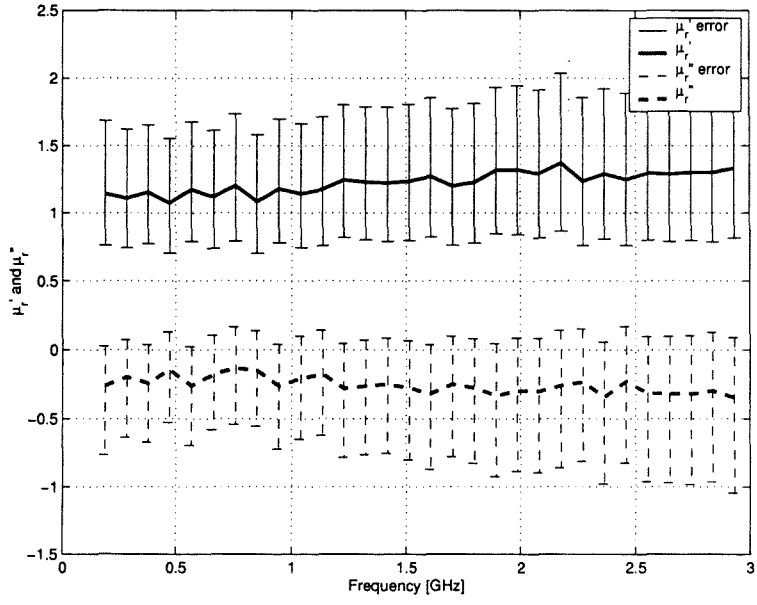

Figure 4.4: μ_r' and μ_r'' of the copper wire showing expected variations from measurement system uncertainties ($\sigma = 5.36 \times 10^7$ S/m).

value for the permeability of copper is $\mu_r = 1 - \mathrm{j}0$ as copper is non-magnetic. The nominal value of μ_r' is at worst 0.37 away from one, while the nominal value for μ_r'' is 0.35 away from zero. The parameter uncertainties give a band of approximately 1.5 for μ_r' and 1 for μ_r'' at 3 GHz. Both bands increase slightly with frequency.

4.2 Unknown Non-magnetic Wire

This unknown wire has a silver-grey colour. It has a measured diameter of 260 μm and a D.C. conductivity of 1.72×10^6 S/m. As a simple check it was held against a powerful magnet and no attractive force was observed.

As the wire is non-magnetic the conductivity can be calculated. This is compared to the D.C. measurement in Fig. 4.5. The maximum error between the least-squares fit and the D.C. measurement is 2.7% at the highest frequency. The inaccuracy of the measurements below 300 MHz is related to gating errors as this is the first 10% of the frequency band, and these points are ignored in the least-squares fit.

The measured and calculated attenuation constants α are compared in Fig. 4.6. The error lies between 3.5% and 7.5%. The graphs show a clear $\sqrt{f}$ dependency indicating that this is a non-magnetic wire and that surface roughness is not a

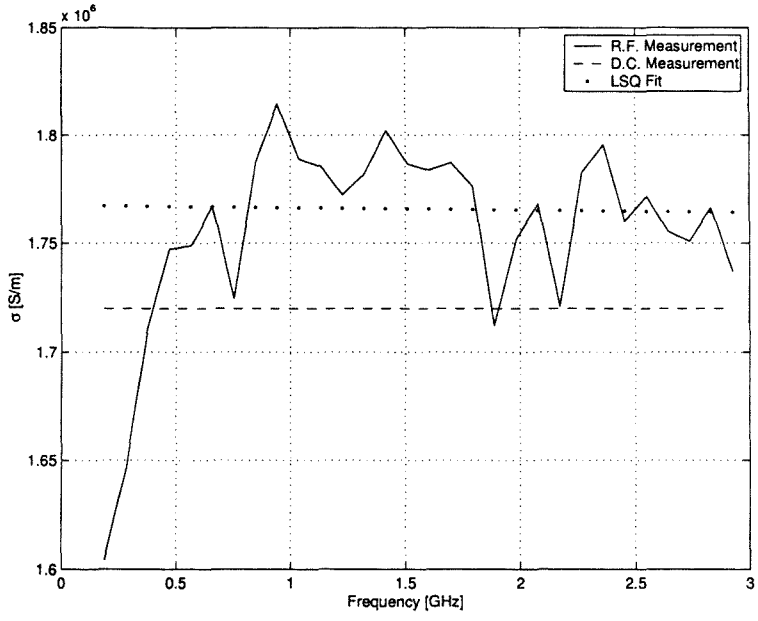

Figure 4.5: Conductivity of the unknown wire comparing the R.F. measurement, with a least-squares fit, to the D.C. measurement.

significant factor.

The measured phase constant β is compared to calculated values in Fig. 4.7. The largest error is approximately 9% at the lower frequencies. This agreement is better than for the copper wire and is because the lower conductivity of the unknown wire makes it less sensitive.

The complex relative permeability μ_r for the unknown wire is shown in Fig. 4.8. Above 300 MHz the largest difference between the nominal value and one for μ_r' is 0.01 while for μ_r'' it is 0.06. This shows good agreement for this non-magnetic wire. The error bands are smaller than for the copper wire as it has a lower conductivity. The bands reach approximately 0.4 for μ_r' and 0.25 for μ_r''.

4.3 Steel Wire

Acoustic guitar steel wire is used in this measurement. The manufacturer states this to be "plain" steel with a diameter of 330 μm and the diameter was confirmed with a digital vernier. A D.C. measurement of conductivity gave 4.17×10^6 S/m.

A guitar wire is approximately 1 m long which required that two wires be connected together to stretch over the 1.5 m of the coaxial cavity. This connection shows in the time domain measurement in Fig. 4.9 as the second reflection

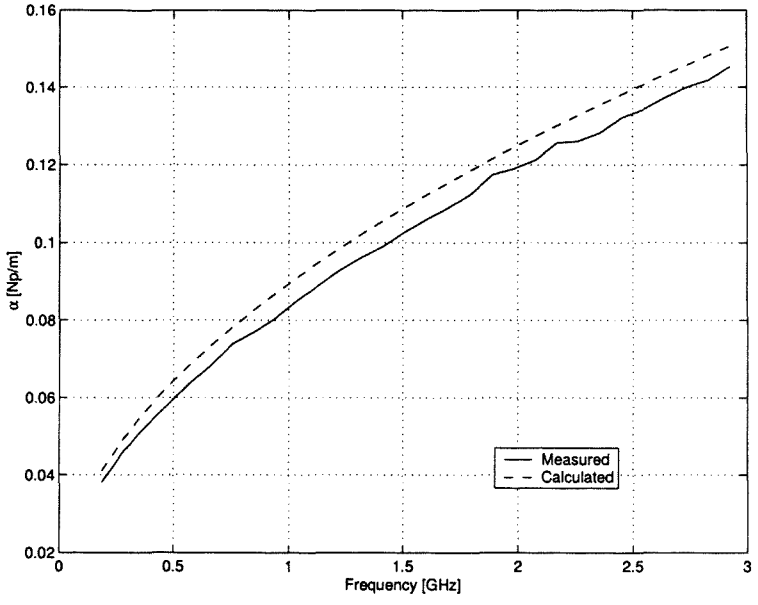

Figure 4.6: Comparison between measured and calculated α of the unknown wire ($\sigma = 1.72 \times 10^6$ S/m).

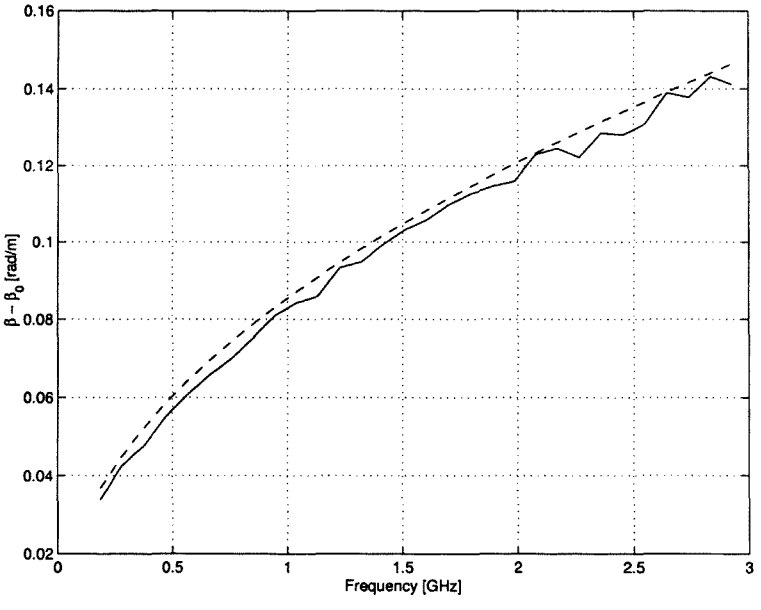

Figure 4.7: Comparison between measured and calculated β of the unknown wire ($\sigma = 1.72 \times 10^6$ S/m).

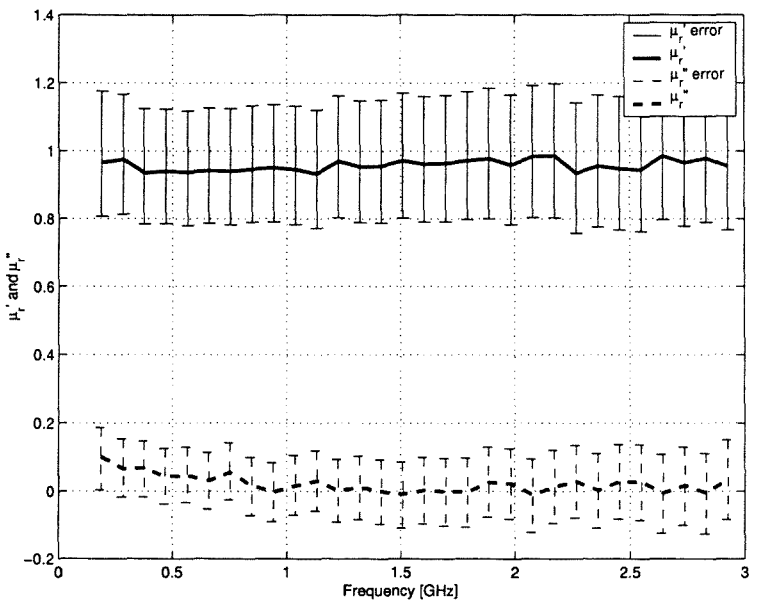

Figure 4.8: μ_r' and μ_r'' of the unknown non-magnetic wire showing expected variations from measurement system uncertainties ($\sigma = 1.72 \times 10^6$ S/m).

at -45 dB and the subsequent secondary reflections. The effect of these small secondary reflections is ignored for the calculation of μ but has an effect on determining the resonant frequency, as can be seen in Fig. 4.11.

The attenuation constant for the steel wire is shown in Fig. 4.10. α no longer shows a $\sqrt{f}$ dependency, indicating that μ is a function of frequency.

The phase constant β of the steel wire is shown in Fig. 4.11. $\beta - \beta_0$ does not show the $\sqrt{f}$ dependency of non-magnetic materials but instead oscillates around a constant value. The oscillations are caused by inaccuracies in determining the resonant frequency by up to 800 kHz. This large error is unexpected and is caused by the cumulative effect of the reflections from the solder connection at 1 m. This was established by taking a continuous (non-magnetic) wire and placing a lump of solder at approximately 1 m. Similar oscillations were observed after the solder was attached.

The relative permeability for the steel wire is shown in Fig. 4.12. The permeability clearly shows that this wire has magnetic properties. The highest value for μ_r' is 17 and for μ_r'' 13, at the lowest frequencies. μ_r' shows a ripple of approximately 1 which is caused by inaccuracies in determining the resonant frequency. The real and imaginary parts of the complex permeability cross at approximately 300 MHz. This crossing behaviour was also observed by Sanderson [7, Fig.18]. The permeability decreases toward 1 as frequency increases as is expected.

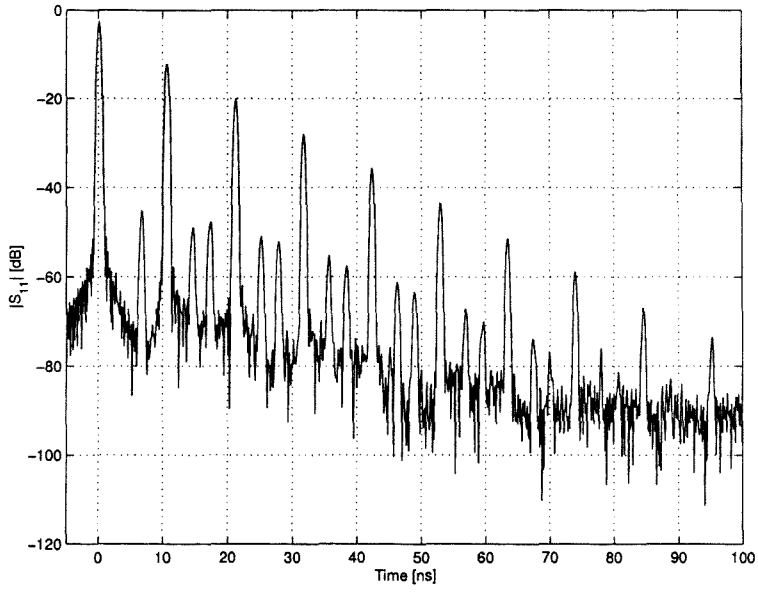

Figure 4.9: S_{11} in the time domain for the steel wire showing the reflections from the connection of two wire lengths at 1 m.

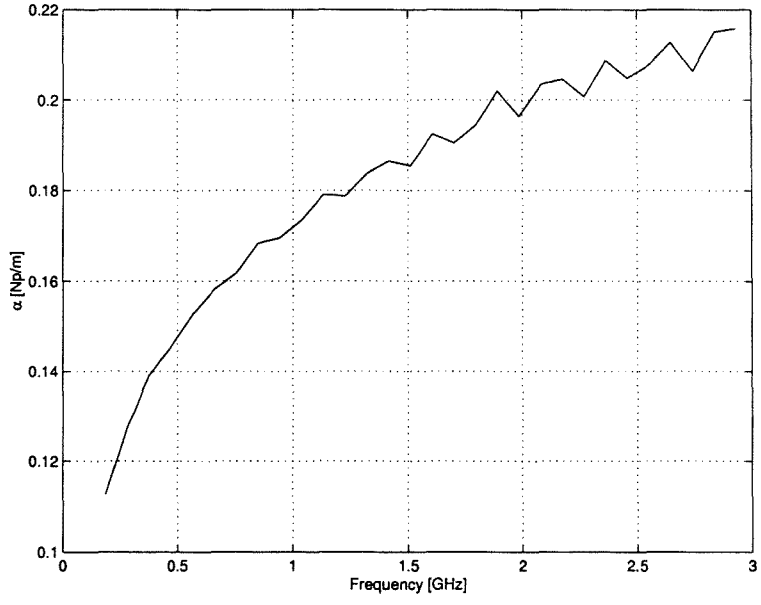

Figure 4.10: Measured attenuation constant α of the steel wire (σ = 4.17×10^6 S/m).

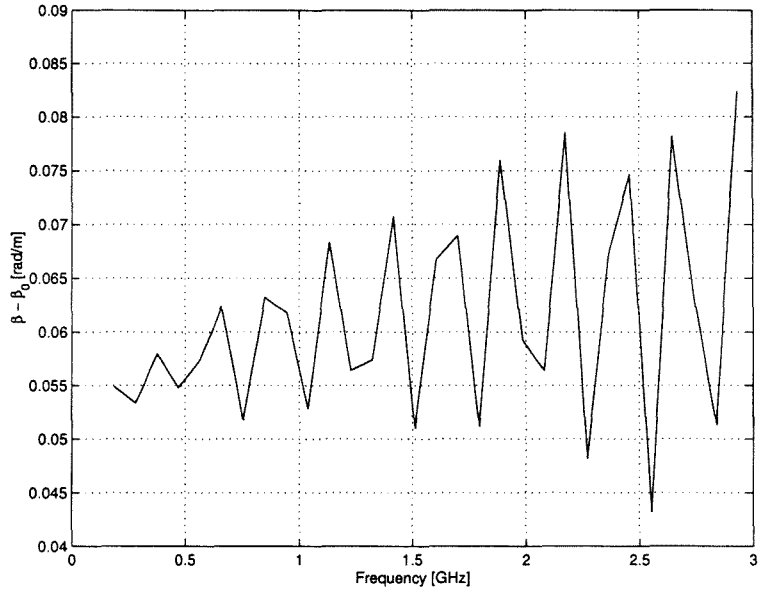

Figure 4.11: Measured phase constant β of the steel wire ($\sigma = 4.17\times10^6$ S/m).

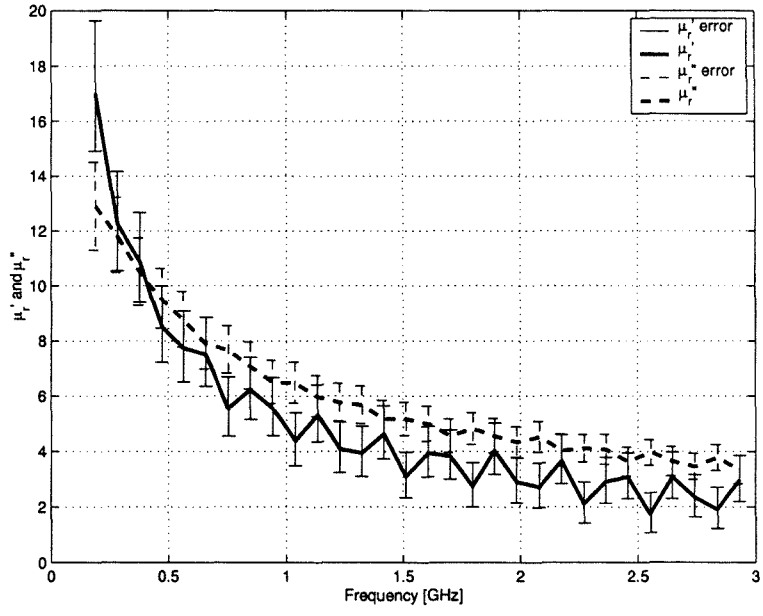

Figure 4.12: The relative permeability μ_r' and μ_r'' of the steel wire ($\sigma = 4.17\times10^6$ S/m).

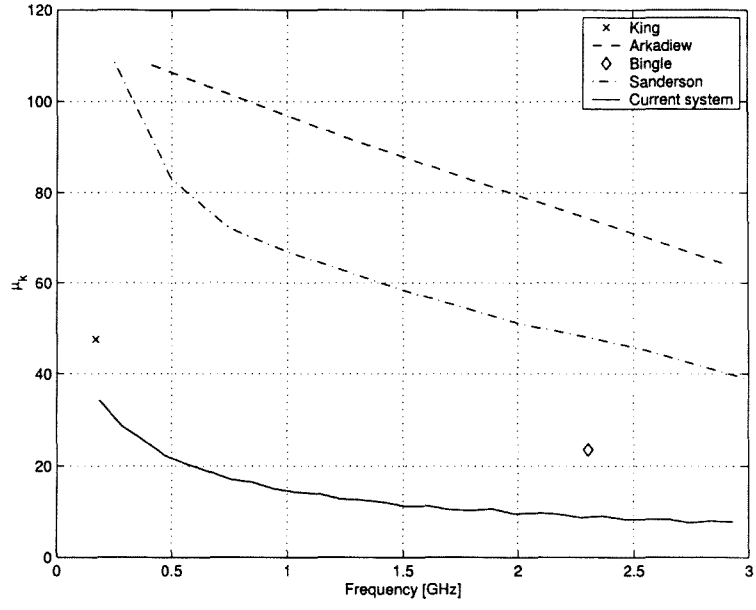

Figure 4.13: Comparison of μ_k of steel wire from various sources: King (from [4, Fig. 5]), Arkadiew [5, Table 17], Bingle [6, p. 1625], Sanderson [7, Fig. 18] and the current measurement system.

The error bands are larger than in the previous non-magnetic measurements, reaching 4.5 for μ_r' and 3 for μ_r'' at the lowest frequencies. The chief causes of this expansion are the uncertainty of radius a and the D.C. conductivity. Note these values are related by the equation for D.C. conductivity (3.72). As the manufacturer's dimensions are matched by a digital vernier measurement it is unlikely that there is such a large variation in a and the error bands at low frequencies can be halved.

Substituting these measured values of μ into the coaxial wavenumber equation (2.50) gives wavenumber values that are the same as the measured α and β, showing that the calculations are also correct for complex permeability. However, there is no simple model for permeability in order to create a theoretical prediction.

In Fig. 4.13 $\mu_k = |\mu| + \mu''$ is compared to other measurements of steel wires. King's wire is simply listed as "No. 21 steel" [4, Fig. 5]. Arkadiew used attenuation methods (discussed in the historical introduction) to measure the permeability of a mild steel wire with 0.187 mm diameter [5, Table 17]. Bingle used steel guitar wire (diameter 300 μm) and found an effective conductivity required to match simulations and measurements of chiral media [6, p. 1625]. Sanderson [7, Fig. 18] used a substitution method to measure the complex permeability of a cold-finished smooth steel rod with a 14 mm diameter.

The graphs shows large variations between the different measurements of different steel wires. This is expected as permeability is very sensitive to the specific chemical composition of the wire, and to other factors listed in §1.1. As there is no standard wire with well-known permeability it becomes impossible to verify a measurement using a single measurement system. The construction of such a standard would be a major contribution to this problem. However, the measurement of non-magnetic wires provides some confidence in the results.

4.4 Conclusion

In this chapter the measurement system was applied to three wires: copper, an unknown non-magnetic wire and steel. For the non-magnetic wires the conductivity at radio frequencies could be measured and compared to the bulk D.C. conductivity. The good agreement (3% – 6%) found suggests that the bulk D.C. conductivity does remain constant over this frequency band as expected from §3.6. The attenuation constant for both these wires followed a $\sqrt{f}$ form, indicating that surface roughness is not a significant factor for these wires. The non-magnetic wires were also found to have a relative permeability of approximately 1 (within 25%), providing confidence in the measurement system.

In order to see the effect of the possible variations of the parameters used to calculate μ realistic extremes for each of the parameters were taken and μ calculated for every possible combination. Error bars on the graphs show the bands of uncertainty around the nominal values. Typically these bars are of the order of 1 and thus the robustness of the measurement system can be considered satisfactory for the measurement of materials with high permeability.

The scalar permeability μ_k of the steel wire was compared to other values from literature. It was found to be much lower, but large variations of steel wire permeability are expected as μ is very sensitive to, amongst other things, specific chemical composition, manufacturing method and magnetic history.

The effect of joining wires is to cause ripple in μ. Even a small reflection from the join (the secondary reflections were 45 dB lower that the signal) causes large variations in β and hence ripple in μ. This suggests that joining wires must be avoided.

The measurement system is thus shown to be working reliably and with sufficient accuracy to be useful.

Chapter 5

Conclusion

In this thesis a novel wideband radio frequency coaxial system was designed for the automatic network analyser measurement of the complex permeability of thin round wires. The wire of interest forms the centre wire of a coaxial system which is terminated with a good short circuit. The measurements were made at room temperature with low field strengths and with no externally applied D.C. magnetic field.

The system requires a calibrated S_{11} measurement which is quick to perform. The measurements do not require two wires with precisely the same diameter, required by the substitution method employed by Sanderson [7] and which can be difficult to manufacture. Substitution errors are thus also avoided.

Evanescent fields at the feed junction of the system were modelled by a capacitance. The time domain gating function of the network analyser was used to determine this capacitance and hence remove its effect. This method of removing the junction effects is quick and does not require the system to be physically altered in any way.

A full wave analysis of the coaxial system was performed using Maxwell's equations. However great simplifications can be achieved by treating the coaxial system as a low-loss transmission line. Surface impedance concepts were used and related to the complex permeability, while half-wavelength resonance was used to find this surface impedance. The worst agreement found between the measured attenuation and phase constants and the full-wave analysis for non-magnetic wires was 31% at the highest frequency, where the system is most sensitive to the length of the coaxial line.

The permeability of a steel wire was measured. The frequency behaviour of the permeability is consistent with measurements reported in the literature, but the magnitude was significantly smaller. This is acceptable as permeability is highly sensitive to chemical composition, manufacturing methods, temperature and magnetic history. Large variations in measured permeability have consistently

been found in the literature.

The measurement system has various limitations. Primarily the system uses low-loss transmission line approximations. Thus a wire with very low conductivity cannot be used in this system. The frequency band is limited at low frequencies by the requirement that the skin depth be much smaller than the circumference of the wire. In general this translates to a minimum frequency of tens of MHz. The upper frequency limit is caused by the cut in of higher order modes. This can be prevented by reducing the size of the outer conductor of the coaxial system. As the radius of the outer conductor becomes smaller its effect on the measurements becomes more pronounced and must eventually be taken into account.

Another limitation of the system is that the time gating requires a sufficient period between reflections from the short circuit termination. This means that the wire must be sufficiently long—approximately 1.5 m for the "maximum" gate shape. This time gate also introduces inaccuracies in the first and last 10% of the band. If the wire is not long enough and a join is necessary ripple in permeability will result.

The measurement system is extremely sensitive to resonant frequency and length. The resonant frequency can be found to a sufficient accuracy by using a linear interpolation. However the length is temperature and humidity dependent and thus high accuracy measurements should be made in a controlled environment. The difficulty of measuring the length with sufficient accuracy can be overcome by measuring the permeability of a known non-magnetic wire and tuning the length until a relative permeability of 1 is found.

The various parameters used to calculate μ were varied to realistic extremes to find the uncertainty bands expected in the measurements. The uncertainty of μ_r was found to be of the order of 1. Reducing the uncertainty would primarily require controlling the temperature and humidity and measuring the diameter of the wire to a higher accuracy.

Future work would include improving the accuracy of the measurements by performing them under controlled environmental conditions. The bandwidth of the system should be increased to make use of the full bandwidth of the network analyser. However it should be noted that sufficiently fine frequency sampling might require several calibrations to cover the full band. Also, increasing the bandwidth requires that the outer conductor diameter be reduced and eventually its surface impedance would have to be taken into account.

The system relies primarily on transmission line resonance phenomena in order to measure surface impedance. It should be possible to apply this technique to a wider range of geometries. The attenuation constant of an arbitrary short-circuited transmission line must create a sufficiently large input resistance at half-wavelength resonance to be measured, while still allowing for low-loss approximations. The transmission line per-unit-length parameters must only be lightly

perturbed by the surface impedance in order for the internal resistance and inductance to be separated from the ideal line parameters. Surface impedance must still be related complex permeability in the same way as in this thesis for the equations to remain valid. Some effort should be spent investigating suitable transmission line candidates for expanding the applicability of the technique.

A significant problem with permeability measurements is the lack of a well known standard. The large variations in Allanson's graphs [4] shows that constructing a standard would be a difficult task. There also seems to be no simple way to find a theoretical permeability for a given material. The construction and measurement of a good reproduceable standard would be a significant contribution to the field of permeability measurements. However, this would also require a second independent measurement system to confirm any measured permeabilities.

In conclusion this thesis presents a technique for measuring complex permeability of thin round wires at radio frequencies. The system has been found to work over a wide band and with sufficient accuracy. The use of a calibrated network analyser allows for highly accurate measurements and thus allows the advancement of techniques of permeability measurements.

Appendix A

Large and Small Argument Bessel Function Approximations

A.1 Large Argument Approximations

Bessel functions with large complex arguments quickly become extremely large [37]. Fortunately, in this work, expressions involving Bessel functions are typically found as ratios of the Bessel function and its derivative, e. g. (2.36). This allows approximations to be made. Harrington [8, Appendix D] lists the large argument approximations for several Bessel functions.

$$J_\nu(z) \xrightarrow[z\to\infty]{} \sqrt{\frac{2}{\pi z}} \cos\left(z - \frac{\pi}{4} - \frac{\nu\pi}{2}\right) \tag{A.1}$$

$$H_\nu^{(2)}(z) \xrightarrow[z\to\infty]{} \sqrt{\frac{2}{\mathrm{j}\pi z}} \mathrm{j}^\nu \mathrm{e}^{\mathrm{j}z} \tag{A.2}$$

If the Bessel functions are written as the ratio of the function to its derivative, as shown below, further approximations can be made.

$$\lim_{z\to\infty} \frac{J_0(z)}{J_1(z)} = \lim_{z\to\infty} \frac{\cos\left(z - \frac{\pi}{4}\right)}{\cos\left(z - \frac{\pi}{4} - \frac{\pi}{2}\right)} \tag{A.3}$$

$$= \lim_{z\to\infty} \frac{\cos\left(z - \frac{\pi}{4}\right)}{\sin\left(z - \frac{\pi}{4}\right)} \tag{A.4}$$

$$= \lim_{z\to\infty} \cot\left(z - \frac{\pi}{4}\right) \tag{A.5}$$

If

$$z = z' - \mathrm{j}z'' \tag{A.6}$$

where z' and z'' are real and positive, then

$$\lim_{z''\to\infty} \cot\left(z' - \mathrm{j}z'' - \frac{\pi}{4}\right) = +\mathrm{j} \tag{A.7}$$

The large argument limit for the Hankel functions is

$$\lim_{z\to\infty} \frac{H_0^{(2)}(z)}{H_1^{(2)}(z)} = \frac{\mathrm{e}^{-\mathrm{j}z}}{\mathrm{j}\mathrm{e}^{-\mathrm{j}z}} \tag{A.8}$$

$$= -\mathrm{j} \tag{A.9}$$

A.2 Small Argument Approximations

Small argument approximations for Bessel functions are given by Harrington [8, p. 203]:

$$J_n(z) \underset{z\to 0}{\longrightarrow} \begin{cases} 1 & \text{if } n = 0, \\ \frac{z^n}{2^n n!} & \text{if } n > 0. \end{cases} \tag{A.10}$$

$$H_n^{(2)}(z) \underset{z\to 0}{\longrightarrow} \begin{cases} -\frac{2\mathrm{j}}{\pi}\ln\left(\frac{\mathrm{j}\gamma z}{2}\right) & \text{if } n = 0, \\ \frac{\mathrm{j}2^n(n-1)!}{\pi z^n} & \text{if } n > 0. \end{cases} \tag{A.11}$$

$$\tag{A.12}$$

where $\gamma = 1,781$.

As the Bessel functions usually appear as a ratio of the function to its derivative, the small argument approximations lead to

$$\left.\frac{J_0(z)}{J_1(z)}\right|_{z \text{ small}} \approx \frac{2}{z} \tag{A.13}$$

and for the Hankel functions

$$\left.\frac{H_0^{(2)}(z)}{H_1^{(2)}(z)}\right|_{z \text{ small}} \approx -z\ln\left(\frac{\mathrm{j}\gamma z}{2}\right) \tag{A.14}$$

Bibliography

[1] R. M. Bozorth, *Ferromagnetism*, D. van Nostrand Company, 1951.

[2] A. Sommerfeld, "Ueber die Fortpflanzung elektrodynamischer Wellen längs eines Drahtes", *Annalen der Physik und Chemie*, vol. 67, no. 2 pp. 233–290, 1899.

[3] J. A. Stratton, *Electromagnetic Theory*, McGraw-Hill, New York, 1941.

[4] J. T. Allanson, "Permeability of ferromagnetic materials at frequencies between 10^5 and 10^{10} cps", *Journal of the Institute of Electrical Engineers*, vol. 92, no. 3 pp. 247–255, 1945.

[5] W. Arkadiew, "Über die Absorption elektromagnetischer Wellen an zwei parallelen Drähten", *Annalen der Physik*, vol. 58, no. 2 pp. 105–138, 1919.

[6] M. Bingle, D. B. Davidson and J. H. Cloete, "Scattering and Absorption by Thin Metal Wires in Rectangular Waveguide — FDTD Simulation and Physical Experiments", *IEEE Transactions on Microwave Theory and Techniques*, vol. 50, no. 6 pp. 1621–1627, June 2002.

[7] A. E. Sanderson, "Effect of Surface Roughness on Propagation of the TEM Mode", in *Advances in Microwaves*, L. Young, ed., Academic Press, New York, vol. 7, pp. 1–57, 1971.

[8] R. F. Harrington, *Time-Harmonic Electromagnetic Fields*, McGraw-Hill, New York, 1961.

[9] J. H. Cloete, M. Bingle and D. B. Davidson, "The Role of Chirality and Resonance in Synthetic Microwave Absorbers", *Int. J. of Electronics and Communications*, vol. 55, no. 4 pp. 233–239, 2001.

[10] J. B. Hoag and H. Jones, "Permeability of Iron at Ultra-Radio Frequencies", *Physical Review*, vol. 42 pp. 571–576, 1932.

[11] J. B. Hoag and N. Gottleib, "The Inner, Initial Permeability of Iron and Nickel from 98 to 410 Megacycles", *Physical Review*, vol. 55 p. 410, 1939.

[12] W. Arkadiew, "On the Permeability of Iron at Ultra-Radio Frequencies", *Physical Review*, vol. 43 pp. 671–672, 1933.

[13] J. L. Glathart, "The Inner, Initial, Magnetic Permeability of Iron and Nickel at Ultra-High Radiofrequencies", *Physical Review*, vol. 55 pp. 833–838, 1939.

[14] D. J. Epstein, "B. Permeability", in *Dielectric Materials and Applications*, A. R. von Hippel, ed., MIT Press, Cambridge, Ma., 1954.

[15] S. Mizutani, T. Yokoshima, H.-S. Nam, T. Nakanishi, T. Osaka and Y. Yamazaki, "High-Frequency Permeability and Thermal Stability of Electrodeposited High-B_s CoNiFe Thin Films", *IEEE Transactions on Magnetics*, vol. 36, no. 5 pp. 2539–2541, September 2000.

[16] U. Raveendranath and K. T. Mathew, "New Cavity Perturbation Technique for Measuring Complex Permeability of Ferrite Materials", *Microwave and Optical Technology Letters*, vol. 18, no. 4 pp. 241–243, July 1998.

[17] M. Ledieu, A.-L. Adenot and O. Acher, "Permeability Measurement of Ferrite Under Stress Up to 6 GHz", *IEEE Transactions on Magnetics*, vol. 36, no. 5 pp. 3254–3256, September 2000.

[18] P.-M. Jacquart and O. Acher, "Permeability Measurement on Composites Made of Oriented Metallic Wires from 0.1 to 18 GHz", *IEEE Transactions on Microwave Theory and Techniques*, vol. 44, no. 11 pp. 2116–2120, November 1996.

[19] S. Ramo, J. R. Whinnery and T. van Duzer, *Fields and Waves in Communication Electronics*, John Wiley & Sons, New York, 3rd edn., 1993.

[20] A. Ishimaru, *Electromagnetic Wave Propagation, Radiation, and Scattering*, Prentice Hall, Englewood Cliffs, New Jersey, 1991.

[21] D. G. Zill and M. R. Cullen, *Advanced Engineering Mathematics*, PWS–Kent, Boston, 1992.

[22] The MathWorks Inc., Matlab 5.3.0.10183 (R11), MATLAB Technical Computing Environment.

[23] G. Goubau, "Surface Waves and Their Application to Transmission Lines", *Journal of Applied Physics*, vol. 21 pp. 1119–1128, November 1950.

[24] The Mathworks Inc., 1999, Matlab Function Reference Volume 1: Language (Online PDF document).

[25] W. C. Chew, *Waves and Fields in Inhomogeneous Media*, Van Nostrand Rienhold, New York, 1990.

[26] G. Goubau, "Single-Conductor Surface-Wave Transmission Lines", *Proceedings of the I.R.E.*, pp. 619–623, June 1951.

[27] Suhner Coaxial Connector Department, *Suhner Coaxial Connectors General Catalogue*, Huber+Suhner AG, Herisau, Switzerland.

[28] Hewlett-Packard HP8510 + 24D, *Student Guide for Basic Network Measurements Using the HP8510B Network Analyser System*, 3rd edn., 1988.

[29] N. Marcuvitz, *Waveguide Handbook*, Peter Peregrinus, London, 1986, (Reprint from 1951).

[30] K. L. Su, *Analog Filters*, Chapman & Hall, London, 1996.

[31] G. Matthaei, L. Young and E. Jones, *Microwave Filters, Impedance-Matching Networks, and Coupling Structures*, Artech House, Norwood, M.A., 1980, (Reprint from 1964).

[32] R. Serway, *Physics for Scientists and Engineers with Modern Physics*, Saunders College Publishing, 1990.

[33] L. V. Blake, "Prediction of Radar Range", in *Radar Handbook*, M. I. Skolnik, ed., McGraw-Hill, Boston, Ma., 2nd edn., 1990.

[34] J. D. Jackson, *Classical Electrodynamics*, John Wiley & Sons, New York, 2nd edn., 1975.

[35] H. A. Haus and J. R. Melcher, *Electromagnetic Fields and Energy*, Prentice–Hall, Englewood Cliffs, New Jersey, 1989.

[36] "UCT Geomatics Programme", 2002, (Course Notes).

[37] C. F. du Toit, "Bessel functions $J_n(z)$ and $Y_n(z)$ of integer order and complex argument", *Computer Physics Communications*, vol. 78 pp. 181–189, 1993.